NISTIR 6204

Neutron Powder Diffraction

United States Department of Commerce
Technology Administration
National Institute of Standards and Technology

NISTIR 6204

Neutron Powder Diffraction

John R. D. Copley
NIST Center for Neutron Research
Materials Science and Engineering Laboratory
National Institute of Standards and Technology

August 1998

U.S. DEPARTMENT OF COMMERCE
William M. Daley, Secretary

TECHNOLOGY ADMINISTRATION
Gary R. Bachula, Acting Under Secretary for Technology

NATIONAL INSTITUTE OF STANDARDS AND TECHNOLOGY
Raymond G. Kammer, Director

Neutron Powder Diffraction

John R.D. Copley,
NIST Center for Neutron Research,
National Institute of Standards and Technology,
Gaithersburg, MD 20899, USA

When a beam of low energy neutrons strikes a material several things can happen. Some will be absorbed, others will emerge in a new direction with or without a change in energy, and the rest will pass through the material unaffected. Those that emerge in a new direction are described as "scattered" neutrons, and the investigation of materials by measuring how they scatter neutrons is known as neutron scattering. Neutron "diffraction", as opposed to scattering, generally implies that there is no attempt to determine the neutron's change in energy when it is scattered. Neutron diffraction is a powerful and popular technique, which is primarily used to determine the crystal structures of materials. It is also used to determine magnetic structures and to study structural properties of non-crystalline solids such as glasses, as well as liquids and dense gases. Bacon (1975) provides a comprehensive discussion of neutron diffraction.

Crystalline solids can be classified according to how the individual crystallites within the material are organized. At one extreme is the single crystal, which consists of one or more crystallites with virtually the same orientation. At the other extreme is the polycrystalline sample in which all possible orientations of crystallites are presumed to be equally likely. A third possibility is the intermediate case of a polycrystalline sample in which the distribution of crystallite orientations is neither uniform nor strongly peaked. This latter type of sample is often described as a sample with preferred orientation or "texture", and an important sub-field of applied neutron diffraction is the study of texture (Prask and Choi, 1993, and references therein). In this lecture we shall only be concerned with experiments on "powders", i.e. polycrystalline samples which are presumed to have a uniform distribution of orientations.

I. General Remarks

I.1. Definitions

A low energy neutron has energy E, wave vector **k**, velocity v, and wavelength λ. These quantities are related as follows:

$$|\mathbf{k}| = \frac{2\pi}{\lambda}; \quad \lambda = \frac{h}{mv}; \quad E = \frac{1}{2}mv^2 = \frac{h^2}{2m\lambda^2}, \tag{1}$$

where h is Planck's constant and m is the mass of the neutron. Approximate conversions are as follows: $E[\text{meV}] \approx \frac{82}{(\lambda[\text{Å}])^2}$, $v[\text{mm}/\mu\text{s}] \approx \frac{4}{\lambda[\text{Å}]}$. The most commonly used unit of neutron energy is the milli-electron volt (meV); 1 meV ≈ 8.1 cm^{-1} ≈ 11.6K ≈ 0.24×10^{12} Hz ≈ 1.6×10^{-15} erg. Note that 1Å=0.1 nm.

In a scattering experiment (fig. 1a), the energy of the incident neutron is E_i and that of the scattered neutron is E_f. (The subscripts "i" and "f" mean "initial" and "final" respectively.) Similarly the incident and scattered wave vectors are $\mathbf{k}_i$ and $\mathbf{k}_f$. The "energy transfer" $\hbar\omega = E_i - E_f$ is the energy transferred to the sample by the neutron when it is scattered. Similarly the "wave vector transfer", or "scattering vector", is $\mathbf{Q} = \mathbf{k}_i - \mathbf{k}_f$. The cosine rule, applied to the $(\mathbf{Q},\mathbf{k}_i,\mathbf{k}_f)$ scattering triangle (fig. 1b), gives $Q^2 = k_i^2 + k_f^2 - 2k_i k_f \cos(2\theta)$, where 2θ is the "scattering angle" (the angle between the incident and scattered neutron beam directions). For the special case of "elastic scattering", i.e. scattering in which the energy of the neutron does not change, $E_i = E_f$, $\hbar\omega = 0$, $\mathbf{k}_i = \mathbf{k}_f$, and $Q = 2k_i \sin\theta = 4\pi \sin\theta / \lambda_i$ where λ_i is the incident wavelength.

I.2. Instrumentation

In a conventional neutron powder diffractometer, at a continuous source such as a research reactor, a beam of monochromatic (single wavelength) neutrons is incident upon a sample and the scattered neutron intensity is measured as a function of the scattering angle 2θ (fig. 2). The monochromatic incident beam is produced by Bragg reflection from an appropriate monochromator crystal. The neutron count-rate is measured in one or more detectors which may or may not be position-sensitive. Collimators restrict the divergence of the beam at various locations; tightening the collimation improves the resolution of the instrument at the expense of intensity.

Another type of neutron diffraction, which we shall not discuss further, is known as "time-of-flight diffraction" (Windsor, 1981). It employs a pulsed beam of polychromatic neutrons and is the technique of choice at pulsed neutron sources.

I.3. Basic Theory

In order to understand the neutron powder diffraction technique, and to compare neutron diffraction with x-ray diffraction, we need to discuss the basic theory of the method (Bacon 1975, Squires 1978, Lovesey 1987).

The atoms in a crystal are periodically arranged. Their positions can be generated by specifying the size and shape of a "unit cell" and the positions of the atoms within the unit cell. The complete structure is obtained by repeating the unit cell many times in all directions. In this section we shall assume that all unit cells are identical (even to the extent that the atoms do not move), that the dimensions of all crystallites are much greater than those of the unit cell, and that complicating effects such as extinction, absorption and multiple scattering can be ignored.

There are two important interactions of neutrons with atoms. They interact with nuclei, and with magnetic moments due to unpaired electrons. For the moment we shall only consider the nuclear scattering.

The scattered intensity in a neutron diffraction experiment on a single crystal is proportional to $I_0 N S(\mathbf{Q})$ where I_0 is the incident beam intensity and N is the total number of atoms in the crystal. The structure factor $S(\mathbf{Q})$ is given by

$$S(\mathbf{Q}) = \frac{1}{N}\left|\sum_{i}^{N} b_i \exp(i\mathbf{Q}.\mathbf{r}_i)\right|^2, \qquad (2)$$

where the sum is over all atoms, $\mathbf{r}_i$ is the position of atom i, and b_i is the "scattering length" or "scattering amplitude" for atom i, which is a measure of the strength of the interaction between the incident radiation and the atom. The periodicity of the crystal lattice implies that $S(\mathbf{Q})$ is zero except at specific values of $\mathbf{Q}$, such that the phase factors $\exp(i\mathbf{Q}.\mathbf{r}_i)$ constructively interfere. These special values of $\mathbf{Q}$, plotted in a 3-dimensional space called "reciprocal space", form a regular grid of points known as the reciprocal lattice. Vectors among these points, called "reciprocal lattice vectors", may be written in terms of three basis vectors $\mathbf{a}^*, \mathbf{b}^*$ and $\mathbf{c}^*$:

$$\mathbf{G}_{hk\ell} = h\mathbf{a}^* + k\mathbf{b}^* + \ell\mathbf{c}^*. \qquad (3)$$

The "Miller indices" h, k and ℓ are integers which characterize the reflection that occurs when $\mathbf{Q} = \mathbf{G}_{hk\ell}$.

The periodicity of the lattice (and the assumption that N is a very large number) enables us to write equation (2) slightly differently:

$$S(\mathbf{Q}) = \frac{(2\pi)^3}{nV}\sum_{G}\delta(\mathbf{Q}-\mathbf{G})\left|\sum_{i}^{n} b_i \exp(i\mathbf{Q}.\mathbf{r}_i)\right|^2. \qquad (4)$$

The first sum is over all reciprocal lattice vectors, the second sum is now restricted to the n atoms in a single unit cell, and V is the volume of the unit cell. For a powder the above result must be averaged over all possible crystallite orientations. The structure factor then becomes a simple function of scalar Q, which vanishes except when Q is equal to the magnitude of one of the reciprocal lattice vectors $\mathbf{G}_{hk\ell}$. Thus the scattering from a powder sample, in an idealized experiment with a mono-directional monochromatic incident beam, is confined to "Debye-Scherrer" cones of scattering at angles 2θ such that $\sin\theta = \lambda_i / 2d_{hkl}$ where the plane spacing $d_{hk\ell} = 2\pi / |\mathbf{G}_{hk\ell}|$.

I.4. Scattering of Neutrons and X-rays

The above discussion, with the same simplifying assumptions, may also be applied to x-ray diffraction.

In comparing the two techniques the first remark that must be made is that the scattered intensity is generally much greater for x-rays than for neutrons because the source is much more intense. It follows that x-ray diffraction is an extremely powerful technique that is frequently preferable to neutron diffraction. Nevertheless there are many situations where the neutron technique is superior and/or complementary in the sense that new information can be obtained by combining the results of measurements using the two techniques.

An important difference between x-rays and neutrons is in the nature of the interaction. The neutron-nucleus interaction is of very short range (of order 10^{-15} m), very much shorter than interatomic distances (of order 10^{-10} m), so that scattering lengths b are independent of Q. On the other hand x-rays interact with electrons and since the spatial

extent of the electron cloud surrounding a nucleus is comparable with interatomic distances the corresponding quantity, which we shall write as f(Q), decreases rather quickly with increasing Q (fig. 3). This quantity, which is called the "atomic scattering factor", is the Fourier transform of the density of electrons surrounding the nucleus. The decrease in f with increasing Q can cause problems in x-ray experiments when there is significant background scattering such as Compton (incoherent) scattering, either from the sample or from the sample environment, since the ratio of signal to background is greatly reduced at high angles.

Another difference between x-rays and neutrons is that for x-rays the forward scattering value of f(Q) is proportional to the number of electrons, i.e. to the atomic number Z, whereas for neutrons there is no simple relationship between the equivalent quantity, b, and the composition of the scattering nucleus. Indeed b varies somewhat erratically with Z, as illustrated in fig. 4. Thus neutrons can sometimes be used to distinguish elements that are close to one another in the periodic table and therefore barely distinguishable in x-ray experiments; a good example is the study of zeolites that contain Al (Z=13, $b=3.5\times10^{-15}$ m) and Si (Z=14, $b=4.2\times10^{-15}$ m). Furthermore it is frequently easier to detect light atoms in the presence of heavy atoms using neutrons rather than x-rays; light elements with significant scattering lengths include H, C, N and O.

The neutron-nucleus scattering length also depends, sometimes dramatically, on the isotope (whereas f(Q) does not). The best known example of the isotope dependence of b involves H and D, whose scattering lengths are -3.8 and $+6.7\times10^{-15}$ m respectively, whereas the value of f(0) is 2.8×10^{-15} m (for both isotopes). The isotope dependence of b has been used to particular advantage in studies of partial distribution functions in liquids and dense gases. There have also been a few reports of the use of isotope substitution in powder diffraction studies.

I.5. Absorption of Neutrons and X-rays

With very few exceptions, x-rays are much more strongly absorbed than neutrons. For example the 1.8Å x-ray and neutron linear absorption coefficients for aluminum are ~21 mm^{-1} and ~0.0014 mm^{-1} respectively. Thus a 150 mm thick aluminum plate has about the same transmission for neutrons as that of a 10 μm thick plate for x-rays (roughly 80%).

The ability of neutrons to penetrate deep within materials can be an important advantage. In studies of materials with compositional gradients, such as cast ingots and coatings, neutron diffraction yields a structure that is representative of the bulk material whereas x-rays provide less useful information, concerning the crystal structure very close to the surface. The ability of neutrons to penetrate materials also opens up the possibility of measuring residual stresses within thick samples; we shall return to this subject in section II.3.

A second important consequence of the low absorption of neutrons is that sample environments for neutron experiments are relatively easy to design, since neutron beams

readily penetrate the various structures that surround devices such as cryostats, furnaces and even high pressure cells; examples are shown in fig. 5.

I.6. Incoherent Scattering

In our discussion of the basic theory we assumed that all unit cells were identical. To the extent that this is untrue the expressions given in section I.3 were not entirely correct. We shall use the word "disorder" to describe situations that cause unit cells to differ from one another, and in this section we shall discuss two types of nuclear disorder. Atomic disorder will be discussed in the following section.

Consider a material that contains one or more elements with more than one stable isotope. Since neutron scattering lengths depend both on Z and on the isotope, the unit cells in this material are not identical and our expression for $S(\mathbf{Q})$ must be modified. For example eq. (2) becomes

$$S(\mathbf{Q}) = \frac{1}{N}\left\{\left|\sum_i^N \langle b_i\rangle \exp(i\mathbf{Q}.\mathbf{r}_i)\right|^2 + \sum_i^N\left[\langle b_i^2\rangle - \langle b_i\rangle^2\right]\right\}, \qquad (5)$$

where angle brackets denote averages over isotopic distributions. The first term in this equation is the Bragg scattering, which is "coherent". The second term, which is independent of Q, is "incoherent" scattering. The strength of the incoherent scattering due to any given atom is proportional to the variance of its scattering length.

Since the neutron has a spin of ½, the interaction of a neutron with a nucleus with nonzero spin I depends on the spin state of the compound nucleus, which is either I+½ or I-½. To the extent that the distribution of nuclear spin directions in a material is random, this produces an additional type of incoherent scattering, which is again independent of Q. Equation (5) still applies, but averages <...> now include nuclear spin states as well as isotopes. The quantities $\sigma_C \equiv 4\pi\langle b\rangle^2$ and $\sigma_I \equiv 4\pi[\langle b^2\rangle - \langle b\rangle^2]$ are called coherent and incoherent scattering cross sections respectively.

Most elements are predominantly coherent scatterers. The most important exceptions are hydrogen and vanadium. The spin-incoherent scattering cross section of hydrogen is a nuisance in diffraction studies since it contributes a large constant background to the measured intensity. For this reason deuterated samples must normally be used. On the other hand the large incoherent scattering cross section of hydrogen can be exploited in inelastic scattering studies of phenomena such as self-diffusion, as we shall see in the lecture about time-of-flight spectroscopy. Since vanadium scatters almost completely incoherently, it is frequently used to make sample containers for powder diffraction experiments; the weakness of its Bragg peaks, due to its very small coherent scattering cross section, is a major advantage which outweighs any disadvantage associated with the incoherent scattering background.

I.7. Atomic Disorder

At least one type of atomic disorder is never absent, no matter how carefully the sample is prepared. This is the thermal disorder that is associated with the motion of atoms about their mean positions. The effect on the scattering is to shift a certain amount of intensity from the Bragg peaks to scattering that is continuous in Q (whereas Bragg scattering

occurs at discrete values of Q). The continuous scattering is sometimes called "thermal diffuse scattering". The equation for the Bragg intensity is modified by replacing b_i with $b_i \exp(-\frac{1}{2}Q^2\langle u_i^2\rangle)$, where the added expression is the so-called temperature factor, or "Debye-Waller factor", for atom i; $\langle u_i^2\rangle$ denotes the mean square displacement of the atom. If the thermal motion is isotropic the temperature factor may also be written as $\exp(-B_i[\sin\theta/\lambda]^2)$, where B_i is the "thermal parameter" for atom i. In many cases the thermal motion is anisotropic, in which case the temperature factor may be considerably more complicated (Willis and Pryor, 1975). Thermal parameters are routinely obtained in the analysis of powder diffraction experiments.

Other kinds of atomic disorder modify the scattered intensity in a diffraction experiment (Guinier, 1963). They include local effects such as compositional disorder, vacancies and interstitials, as well as more extended phenomena such as dislocations, grain boundaries, clusters and pores. The larger scale structures are generally better studied using the small angle scattering technique whereas smaller scale objects show up better in diffraction experiments. Defects generally modify the Bragg scattering and contribute to the diffuse scattering between the Bragg peaks. The Bragg peaks may be modified in intensity, position and/or width, and the different ways that these modifications depend on the reflection can be used to distinguish among the various phenomena. For example line broadening can be due to the small size of the crystallites in the sample, in which case it is independent of Q, or it can be due to the effects of strains, in which case it increases with increasing Q.

I.8. Magnetic Scattering

We have seen that neutrons interact with nuclei. Because of their magnetic moment they also interact with magnetic moments on atoms with unpaired electrons (Furrer 1995). The magnetic interaction of neutrons is more complicated than the nuclear interaction, and we shall only consider the simplest of situations. For a detailed discussion see Izyumov and Ozerov (1970).

A crystalline material with an ordered magnetic structure (e.g. a ferromagnetic or anti-ferromagnetic material), placed in a neutron beam, produces magnetic Bragg peaks in addition to the nuclear Bragg peaks previously discussed. If the beam is unpolarized the nuclear and magnetic structure factors, $S(\mathbf{Q})$ and $S_M(\mathbf{Q})$, add in the following way:

$$S_{tot}(\mathbf{Q}) = S(\mathbf{Q}) + S_M(\mathbf{Q})\sin^2\alpha, \qquad (6)$$

where α is the angle between the magnetization vector and the scattering vector. The expression for $S_M(\mathbf{Q})$ is similar to equation (2), except that b_i is replaced with the quantity $p_i(Q) = A_i f_i^M(Q)$ where A_i is proportional to the magnetic moment of atom i and $f_i^M(Q)$ is its magnetic form factor. For a powder the coefficient $\sin^2\alpha$ is replaced by its average value, which is 2/3.

Single crystal and powder diffraction experiments using unpolarized neutrons can be used to determine magnetic structures as well as conventional crystal (chemical) structures. Magnetic moments can also be determined. More sophisticated experiments using polarized neutron beams and/or polarization analysis of the scattered neutrons, with

or without a magnetic field applied to the sample, yield more detailed information about a material.

I.9. Rietveld Profile Refinement

The standard method of analyzing the results of a neutron powder diffraction experiment, known as "Rietveld profile refinement" and named for the person who developed the method, is to fit the parameters of a model to the measured "profile", which is the intensity measured as a function of scattering angle 2θ. A typical measurement and the fitted profile are shown in fig. 6. The Rietveld technique is discussed in Young (1993).

The model parameters in a Rietveld refinement can be divided into several categories, according to what aspect of the profile they describe. First of all, and most importantly, there are the parameters that determine the positions and intensities of the Bragg peaks themselves, i.e. the parameters that describe the crystal structure. These include the cell parameters themselves, the positions of the atoms within the unit cell, site occupancies, and thermal parameters. Next there are parameters that describe the so-called "background", which is the relatively smooth scattering that lies between and below the Bragg peaks. This can include diffuse elastic coherent scattering and inelastic and/or incoherent scattering from the sample and its environment, plus the "true" background, which includes contributions due to air scattering, electronic noise, and other unwanted sources. The Bragg peaks, which correspond to elastic scattering that occurs at well-defined scattering angles, can usually be separated from the background because the background scattering varies rather slowly with scattering angle whereas the Bragg scattering is highly structured. A third set of parameters describes the widths of the peaks. Line broadening is in part due to the resolution of the instrument itself, which is generally a well-parametrized function of 2θ for a given instrumental configuration. There may also be contributions to the broadening due to size and strain effects. The results of neutron diffraction experiments at a reactor are generally easier to refine than results from other sources because peak shapes tend to be simpler and fewer corrections need be applied.

II. Applications

We now discuss applications of the neutron diffraction technique to materials of industrial interest. We conclude with a brief discussion of neutron experiments on C_{60}.

II.1. High Temperature Superconductors

It goes without saying that there is great interest in the development of high temperature superconductors for commercial applications. Neutron diffraction has played a very important rule in elucidating the structures of these materials, in large part because of the crucial role played by the oxygen vacancies and the greatly improved visibility of oxygen in the presence of heavy elements when compared with x-ray diffraction. Furthermore the ability of neutrons to penetrate bulk samples, with very little absorption, simplifies the data analysis considerably. Structural information from neutron scattering

experiments has helped us improve our understanding of the crucial role of the oxygen defects in high temperature superconductors.

The mercury superconductors $HgBa_2Ca_{n-1}Cu_nO_{2n+2+\delta}$ have generated considerable interest in the superconductivity community. The oxygen dependence of the structure of the single layer material $HgBa_2CuO_{4+\delta}$, with $0.04 \leq \delta \leq 0.23$, and its effect on the superconducting phase transition, have been studied using the neutron powder diffraction method (Huang et al, 1995). The measurements were performed using the 32-detector high-resolution powder diffractometer at the NIST research reactor. The incident wavelength was 1.539Å, obtained by Bragg reflection from a Cu(311) monochromator crystal. Collimations before and after the monochromator (cf. fig. 2) were 15' and 20' FWHM (full width at half maximum) respectively, and 7' FWHM collimators were placed between the sample and each detector. The powders, in amounts of the order of 4 g, were contained in thin-walled (0.15 mm) vanadium cans which were mounted in a closed cycle helium refrigerator (cf. fig. 5). Scans were recorded for scattering angles 2θ from 8° to 145°, and counting times were roughly 8 hours at each temperature. The crystal structure (fig. 7) remains tetragonal over the whole range of δ, and at all temperatures from 10K to 300K. The excess oxygen is found to occupy so-called O(3) sites in the Hg layers. The thermal parameters for the Hg and Ba atoms were highly anisotropic, such that the corresponding real space thermal ellipsoids (which characterize the probability of finding an atom at a particular location relative to its equilibrium position) are respectively oblate (squashed) and prolate (egg-shaped). This finding suggests that the positions of the Hg and Ba atoms are strongly influenced by the presence or absence of an oxygen atom at the O(3) site. With regard to the Ba atoms, the conjecture is confirmed by results for the distances of the Ba atoms from various oxygen sites in the structure, and by the success of a model that postulates two partially occupied Ba sites, such that the sum of the occupancies is unity, at slightly different distances from the Cu planes. The ratio of the Ba thermal parameters B_{33}(Ba) and B_{11}(Ba), respectively normal and parallel to the tetragonal planes, is shown in fig. 8(a) as a function of δ. This curve is remarkably similar to the plot of T_c as a function of δ which is shown in fig. 8(b), suggesting a correlation between T_c and the displacements of the Ba atoms.

II.2. Colossal Magnetoresistors

The resistivity of a magnetic material changes when it is placed in a magnetic field. The effect is generally small, and best observed at low temperature. In some materials the effect is anisotropic, i.e. the resistance changes when the current flowing through the material is changed from being parallel to the internal magnetization to being perpendicular to it. Typically the change in resistance on changing the current direction is of order 1 or 2 % at most. A good example is permalloy ($Ni_{0.8}Fe_{0.2}$), where the anisotropic magnetoresistance effect is used in device applications such as read heads for computer hard disk drives.

About 10 years ago a much larger effect, dubbed "giant magnetoresistance" (GMR), was discovered in an iron-chromium magnetic superlattice. GMR materials have alternating layers of ferromagnetic and non-magnetic metals deposited on an insulating substrate, and the resistance parallel to the layers is largest (its value is R_0) when the magnetic moments in the ferromagnetic layers alternate from one layer to the next (in the absence

of an applied field). On the other hand the resistance is smallest (R_∞) when the layers are parallel to one another (when the field saturates the magnetization). In the past few years GMR research has advanced rapidly, with new materials being developed; the current record for the resistance ratio R_0/R_∞ is $\approx$3.2. Much of the recent GMR research has been driven by a desire to develop a new generation of read heads for computer hard disk drives. A continuing challenge is to manufacture devices that can read increasingly high bit densities. Other types of devices that are candidates for development using GMR materials include magnetic memory chips, magnetic transistors, motion sensors, and sensor arrays for land mine detection.

A somewhat different phenomenon, called "colossal magnetoresistance" (CMR), was first reported in 1994. CMR materials have truly enormous resistance ratios, some being well in excess of 1000. Indeed the change in resistance that occurs when a CMR material is placed in a sufficiently high magnetic field is greater than the change produced when a high temperature superconductor is cooled through its superconducting transition temperature! The resistance of a CMR material drops enormously when the spins order ferromagnetically, either when the temperature is lowered or when a magnetic field is applied. This large variation in carrier mobility originates from a metal-insulator transition that is closely associated with the magnetic ordering. The most well-known CMR materials are the calcium-doped lanthanum manganites $La_{1-x}Ca_xMnO_3$, and the compound with x=0.33, which we may write as $La^{3+}_{0.67}Ca^{2+}_{0.33}Mn^{3+}_{0.67}Mn^{4+}_{0.33}O_3$, shows the most dramatic magnetoresistance effect. The undoped material, $LaMnO_3$, is antiferromagnetic but it can be converted to a ferromagnet in an oxidizing atmosphere. This is also true of materials with small x, but at larger values of x the materials are ferromagnetic, no matter how they are prepared.

Much of our understanding about the relationship between the magnetoresistive properties of these materials and their structures has come from neutron powder diffraction experiments. The experiments that we shall very briefly describe were part of a comprehensive study of the crystal and magnetic structures of $La_{1-x}Ca_xMnO_3$ compounds with $0<x\leq0.33$. In order to resolve a discrepancy regarding the magnetic ordering in low concentration Ca-doped manganites, Huang et al (1997) looked at two such materials with x=0.06. The first sample, which we shall call the oxidized sample, was prepared in air at 1350°C by mixing appropriate quantities of La_2O_3, $MnCO_3$ and $CaCO_3$. The other sample, described as reduced, was prepared from the first sample by annealing at 900°C in a reducing atmosphere. The reduced sample, whose chemical formula may be written as $La_{0.94}Ca_{0.06}Mn^{3+}_{0.94}Mn^{4+}_{0.06}O_3$, had all atomic sites fully occupied whereas the oxidized sample had cation vacancies; its approximate chemical formula was $(La_{0.94}Ca_{0.06}Mn^{3+}_{0.69}Mn^{4+}_{0.31})_{0.96}O_3$. The reduced sample was antiferromagnetic at low temperatures, in common with the undoped compound $LaMnO_3$, but the oxidized sample was ferromagnetic, since a far greater proportion of the Mn ions were in the +4 valence state. The orthorhombic crystal structure is illustrated in fig. 9, together with the magnetic ordering in the ferromagnetic and antiferromagnetic states. Figs. 10 and 11 show refinements of the structures of the reduced and oxidized compounds. In each of these figures the upper part of the inset shows the low angle data, represented by symbols, and the calculated profile for the crystal structure alone. The

lower part of each inset shows the difference, which represents the magnetic scattering. We see from these figures that the reduced compound has peaks that are purely magnetic whereas the oxidized sample does not. The oxidized compound is ferromagnetically ordered as in fig. 9(c), whereas the reduced sample is antiferromagnetically ordered as in fig. 9(d).

II.3. Residual Stress Measurements

One of the best examples of an applied research area that benefits from neutron diffraction is the study of residual stresses in materials (Prask and Brand, 1997). The neutron method is non-destructive and capable of relatively deep penetration within many materials. The non-destructive nature of the technique is especially important because the act of cutting into a material in order to perform a destructive measurement can actually modify the stresses that the measurement was intended to determine.

A typical experimental setup is shown in fig. 12. The incident and diffracted beams are not only well collimated (restricted in direction) but also limited in lateral extent using neutron-absorbing masks. Thus the only once-diffracted neutrons that can enter the detector are those that were scattered within a "gauge volume" defined by the intersection of the incident and diffracted beams. The optimum setup occurs when the scattering angle is 90°. By translating the sample within the beam, different gauge volumes can be examined.

Residual stresses are not directly measured in these experiments (nor using any other experimental technique). Writing the Bragg equation as $\lambda = 2d\sin\theta$, the mean d-spacing within the gauge volume, d, is determined from the angular position of the observed Bragg peak. The local strain is $(d-d_0)/d_0$, where d_0 is the unstressed d-spacing. Stresses are computed using the diffraction elastic constants for the reflection.

Many residual stress studies have been undertaken over the past 15 years, and dedicated facilities are now found at neutron scattering centers in North America, Europe and Asia. Systems that have been studied include weldments, ceramic coatings, composites, reference specimens, turbine blades, and various military components. An example that illustrates the technique is a recent study of residual stresses in a thin (6.35 mm thick) section of railroad rail (Brand et al, 1996). The experimental setup at the NIST research reactor is shown in fig. 13. Measurements were made using a ≈2.4 mm ×2.4 mm ×2.4 mm gauge volume, at a mesh of points that were 5 mm apart in orthogonal x and y directions normal to the length of the uncut rail. Measurements of 5 different d-spacings, in five different orientations at each of the mesh points, were used to extract four components of the residual stress tensor. A typical result is shown in fig. 14.

The results of these types of experiments are typically compared with the results of model calculations, enabling engineers to improve their models. They are also compared with the results of other types of experimental investigations, some of which may have the advantage that they are relatively inexpensive though they may not be as accurate. The ultimate objective is to be able to predict performance with reasonable accuracy, thereby improving economy and durability.

II.4. Carbon-60

Buckminsterfullerene, C_{60}, was discovered in 1985, and a method of making macroscopic samples was reported about five years later. Since that time there has been considerable research activity in many different fields. One of the more fundamental problems has been to understand the structure of solid C_{60}, and some of the most useful information has come from diffraction experiments using neutrons (Copley et al, 1992). One of the reasons that neutrons have been so useful in structure studies of C_{60} has to do with the very high symmetry of the molecule. The scattering due to an icosahedral C_{60} molecule appears at relatively high Q, which is where the atomic scattering factor for x-rays, f(Q), is small so that signal-to-background becomes problematic in x-ray experiments.

Solid C_{60} is crystalline, with icosahedral molecules located at face-centered cubic lattice sites. The nearest neighbor distance between molecular centers is approximately 10Å. The room temperature diffraction pattern, shown in fig. 15, only has peaks at positions where peaks are predicted on the assumption that all molecules are structurally equivalent. On the other hand the low temperature diffraction pattern, shown in fig. 16, has additional peaks which imply that the molecules have become structurally inequivalent. A reasonable first approximation to the crystal structure of C_{60} is that below the first order orientational order-disorder transition temperature, T_1~260K, each molecule adopts one of four possible orientations such that the unit cell is a simple cube containing four molecules (fig. 17), whereas above T_1 the molecules are randomly oriented.

The reader will have noticed that the relatively smooth "background" under the room temperature diffraction pattern (fig. 15) is intense, and curiously structured. It is in fact diffuse scattering which can be rather well explained as a consequence of the orientational disorder that is postulated to explain the Bragg peaks. Indeed the complete diffraction pattern (Bragg peaks plus diffuse scattering) can be described by a very simple model which assumes that all molecular orientations are equally likely. This picture of room temperature C_{60} is certainly oversimplified, since the icosahedral symmetry of the C_{60} molecule and the cubic symmetry of the lattice must at some level influence the distribution of molecular orientations. To gain a better understanding of what is going on requires a multi-pronged approach, involving theory (e.g. Michel and Copley, 1997), computer simulations and experiments. Both neutrons and x-rays have been used, and there have been studies of powder samples and single crystals. The goal is to develop an improved representation of the interactions between the molecules in this fascinating material.

Our description of the low temperature structure is also woefully incomplete. Powder neutron diffraction data (David et al, 1992) have shown that each molecule adopts two types of orientations (fig. 18), described as "pentagon-facing" and "hexagon-facing", and that the probability p that a molecule adopts the pentagon-facing orientation increases

with decreasing temperature, as shown in fig. 19. Below ~86K, p no longer changes with temperature, indicating that the system has frozen into an orientational glass.

The work described in the previous paragraph was performed using a time-of-flight diffractometer at a pulsed neutron source. Such instruments are well suited to measurements at large Q. A good example is a study of the structure of the C_{60} molecule itself, using data obtained up to Q-values as high as 50 $Å^{-1}$ (Soper et al, 1992). The extended range of Q was needed in order to be able to convert the data to a real space pair correlation function.

The picture that emerges from a diffraction experiment corresponds to the average of a series of instantaneous "snapshots" of the system. Thus a diffraction experiment on C_{60} cannot determine whether the orientational disorder that is clearly apparent above the phase transition is static or dynamic. In the lecture about time-of-flight spectroscopy we shall describe inelastic neutron scattering measurements that allow us to make such a distinction, affording additional insights into the behavior of the molecules in this fascinating material.

Acknowledgments

It is a pleasure to thank my colleagues at NIST, especially Julie Borchers, Paul Brand, Jeremy Cook, Qing-Zhen Huang, Jeff Lynn, Dan Neumann, Hank Prask, Louis Santodonato, Tony Santoro, and Brian Toby, for useful discussions, for the use of figures, and for the use of unpublished results.

References

G.E. Bacon (1975), "Neutron Diffraction", 3rd Ed. (Oxford University Press, Oxford).

P.C. Brand, H.J. Prask and G.E. Hicho (1996), National Institute of Standards and Technology Internal Report NISTIR-5912.

J.R.D. Copley, D.A. Neumann, R.L. Cappelletti and W.A. Kamitakahara (1992), J. Phys. Chem. Solids 53, 1353.

W.I.F. David, R.M. Ibberson, T.J.S. Dennis, J.P. Hare and K. Prassides (1992), Europhys. Lett. 18, 219 and 735.

A. Furrer (1995) (ed.), "Magnetic Neutron Scattering" (World Scientific, Singapore).

A. Guinier (1963), "X-ray Diffraction in Crystals, Imperfect Crystals, and Amorphous Bodies" (W.H. Freeman, San Francisco and London).

Q. Huang, J.W. Lynn, Q. Xiong and C.W. Chu (1995), Phys. Rev. B52, 462.

Q. Huang, A. Santoro, J.W. Lynn, R.W. Erwin, J.A. Borchers, J.L. Peng, K. Ghosh and R.L. Greene (1997), Phys. Rev. B (submitted).

Yu.A. Izyumov and R.P. Ozerov (1970), "Magnetic Neutron Diffraction" (Plenum, New York).

S.W. Lovesey (1987), "Theory of Neutron Scattering from Condensed Matter" (Oxford University Press, Oxford).

K.H. Michel and J.R.D. Copley (1997), Z. Phys. B103, 369.

H.J. Prask and P.C. Brand (1997), in "Neutrons in Research and Industry", ed. G. Vourvopoulos, SPIE Proceedings Vol. 2867, p. 106.

H.J. Prask and C.S. Choi (1993), in "Concise Encyclopaedia of Materials Characterization", eds. R.W. Cahn and E. Lifshin (Pergamon Press, Oxford), p. 497.

A.K. Soper, W.I.F. David, D.S. Sivia, T.J.S. Dennis, J.P. Hare and K. Prassides (1992), J. Phys.: Condens. Matter 4, 6087.

G.L. Squires (1978), "Thermal Neutron Scattering" (Cambridge University Press, Cambridge).

B.T.M. Willis and A.W. Pryor (1975), "Thermal Vibrations in Crystallography" (Cambridge University Press, Cambridge).

C.G. Windsor (1981), "Pulsed Neutron Scattering" (Taylor and Francis, London).

Q. Xiong, Y.Y. Xue, Y. Cao, F. Chen, Y.Y. Sun, J. Gibson, C.W. Chu, L.M. Liu and A. Jacobson (1994), Phys. Rev. B50, 10346.

R.A. Young (1993) (ed.), "The Rietveld Method" (Oxford University Press, Oxford).

Figure Captions

Fig. 1. A scattering event in real space (a), and the corresponding scattering triangle (b). The symbols are defined in the text.

Fig. 2. A schematic drawing of a diffractometer, showing the reactor source, the monochromator crystal, the sample, and two detectors. Collimators are placed before and after the monochromator crystal and between the sample and each detector. The NIST diffractometer has 32 detectors, at angular intervals of 5°; the complete array of detectors and collimators can be rotated about a vertical axis through the sample table.

Fig. 3. The neutron scattering length of carbon, which is independent of Q, and the corresponding x-ray atomic scattering factor, f(Q).

Fig. 4. The variation of neutron scattering length b with atomic number Z, for the naturally occurring elements.

Fig. 5. Examples of sample environments. At (a) is a popular low temperature setup, capable of sample temperatures of order 10K. The sample is bolted to the cold stage of a closed cycle helium refrigerator. There are two heat shields and an outer vacuum vessel, all made of aluminum. At (b) is a schematic drawing of a high pressure cell, made of a high strength aluminum alloy and capable of operating pressures up to ~620 Mpa (~6100 atmospheres). At (c) is a schematic drawing of an 1800°C furnace, designed at the Institut Laue-Langevin, Grenoble, France. At beam height the heater consists of two concentric 0.02 mm thick Nb foils, the eight heat shields are also 0.02 mm Nb foils, and the outer vacuum jacket is made of ≈1.5 mm thick aluminum. At left, at beam height, is a vertical piece of tubing that carries cooling water to and from the lower part of the furnace; the furnace is normally rotated so that the tubing does not interfere with the incident or scattered beams.

Fig. 6. The high angle part of the neutron powder diffraction pattern of cubic $LaBa_2Fe_3O_{9-\delta}$, measured at 295K. The incident wavelength was 1.54Å, obtained using a Cu(311) monochromator. Notice that the widths of the peaks, which are very largely due to the resolution of the instrument, depend on the scattering angle 2θ. Points represent the data and the line through the data represents the result of the profile refinement. The difference between experiment and calculation is shown at the bottom, and the small vertical lines indicate the positions of the calculated peaks.

Fig. 7. The tetragonal crystal structure of $HgBa_2CuO_{4+\delta}$. Doping occurs on the partially occupied O(3) sites.

Fig. 8. (a) The ratio of the out-of-plane (B_{33}) and in-plane (B_{11}) thermal parameters for the Ba atoms in $HgBa_2CuO_{4+\delta}$. (b) The dependence of the superconducting transition temperature T_c on δ for $HgBa_2CuO_{4+\delta}$. Also shown is the dependence of T_c on the hole concentration (the number of carriers per Cu), from measurements by Xiong et al (1994).

Fig. 9. The orthorhombic crystal structure of $La_{1-x}Ca_xMnO_3$ is shown in (a) and the tilting of the MnO_6 octahedra is shown in (b). The orientations of the Mn magnetic moments are shown in (c) and (d) for the ferromagnetic and antiferromagnetic structures respectively.

Fig. 10. Rietveld refinements of neutron diffraction data for the stoichiometric reduced compound $La_{0.94}Ca_{0.06}MnO_3$ at 12K. The points are the data and the line through the points is the refinement. The Bragg peak positions are shown as short vertical lines. At the bottom is shown the difference between the data and the calculated profile. The inset shows the low angle data together with the calculated profile for the nuclear contribution to the diffraction pattern; the magnetic contribution shows up in the difference plot at the bottom of the inset.

Fig. 11. Rietveld refinements of neutron diffraction data for the oxidized compound $(La_{0.94}Ca_{0.06})_{0.97}Mn_{0.97}O_3$ at 12K. The points are the data and the line through the points is the refinement. The Bragg peaks positions are shown as short vertical lines. At the bottom is shown the difference between the data and the calculated profile. The inset shows the low angle data together with the calculated profile for the nuclear contribution to the diffraction pattern; the magnetic contribution shows up in the difference plot at the bottom of the inset.

Fig. 12. A schematic representation of the experimental setup for a residual stress measurement. The incident and scattered beams are well collimated and spatially restricted using neutron-absorbing masks.

Fig. 13. The actual experimental setup for the determination of residual stresses in a slice of railroad rail, using the BT8 spectrometer at the NIST research reactor. The incident beam tube is at the top and the collimation system for the diffracted neutrons is at the lower right of the picture.

Fig. 14. A contour map showing the residual stress σ_{xx} in the rail head (in MPa). The x direction is horizontal, normal to the length of the rail. Distances are in inches: 1 inch = 25.4 mm.

Fig. 15. Parts of the room temperature powder neutron diffraction pattern for C_{60}. Points represent the measurements and the solid line represents a calculation assuming that molecules are located on a face-centered cubic lattice, randomly oriented. Difference plots are also included.

Fig. 16. Parts of the low temperature powder neutron diffraction pattern for C_{60}. Points represent the measurements and the solid line represents a calculation which assumes that each molecule adopts one of two possible orientations, pentagon-facing with probability 0.83 and hexagon-facing with probability 0.17, such that there are four molecules in the simple cubic unit cell. Difference plots are also included.

Fig. 17. The crystal structure of C_{60}. At all temperatures the molecules are located at face-centered cubic lattice sites. Above the phase transition they adopt many different orientations. At low temperatures there are four molecules in the unit cell, each with a different orientation. Each type of orientation, be it pentagon-facing or hexagon-facing, is obtained by rotating the molecules from their "standard" orientations (with 2-fold axes pointing along cube edge directions, as shown in the figure) through the same angle but about different (111) axes, as shown. For the pentagon-facing orientation the angle is about 98°; for the hexagon-facing orientation it is ≈38°.

Fig. 18. Relative orientations of nearest neighbor C_{60} molecules in the low temperature phase. Part of a neighboring molecule is viewed from within the molecule at the origin. The pentagon-facing orientation is shown at (a) and the hexagon-facing orientation is shown at (b). In each case the polygon (pentagon or hexagon) faces a hexagon-sharing "double bond" on the neighboring molecule.

Fig. 19. The temperature dependence of the probability of the pentagon-facing orientation in low temperature C_{60} as derived from neutron diffraction experiments.

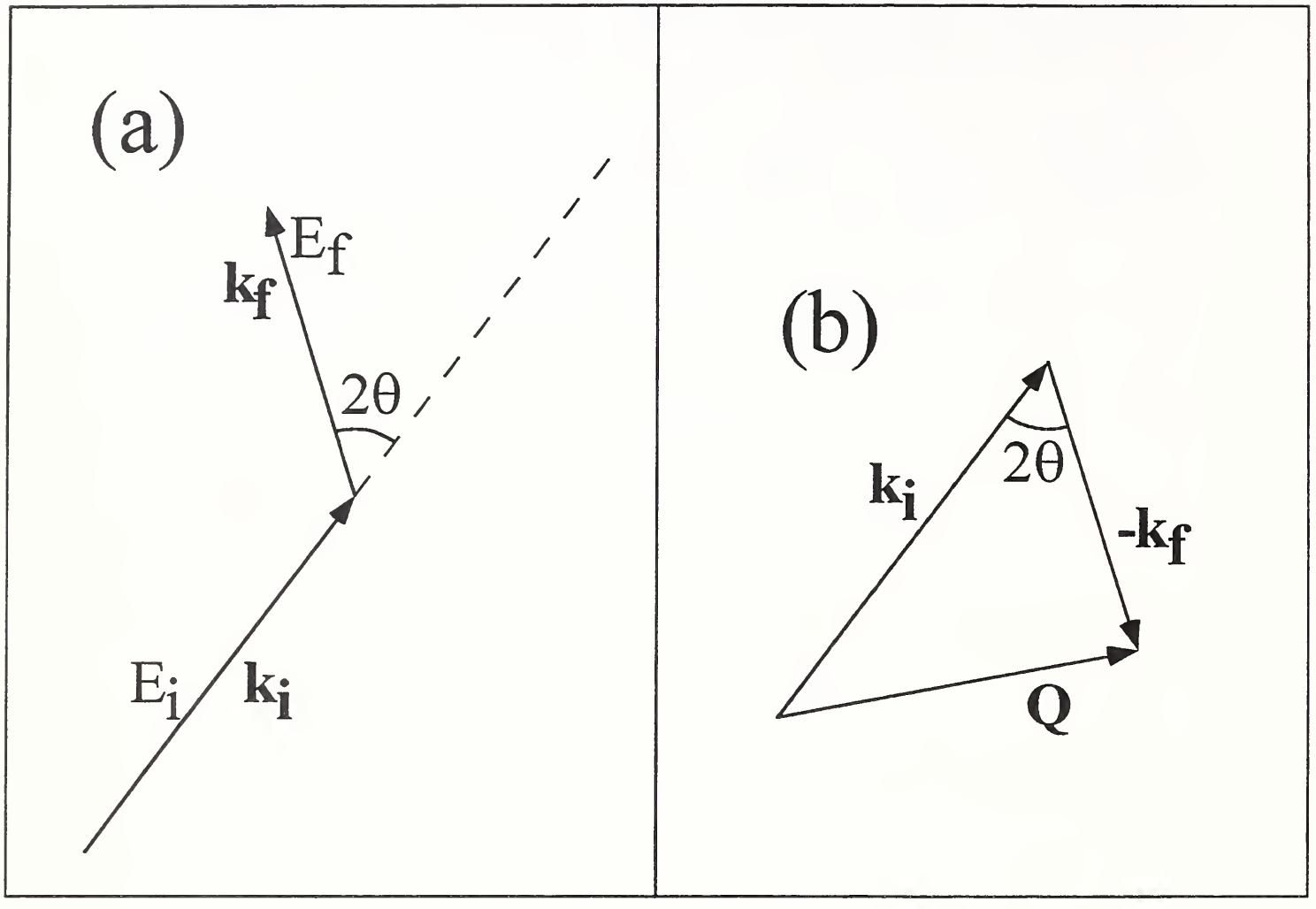

$$\hbar\omega = E_i - E_f$$

$$\mathbf{Q} = \mathbf{k}_i - \mathbf{k}_f$$

Fig.1

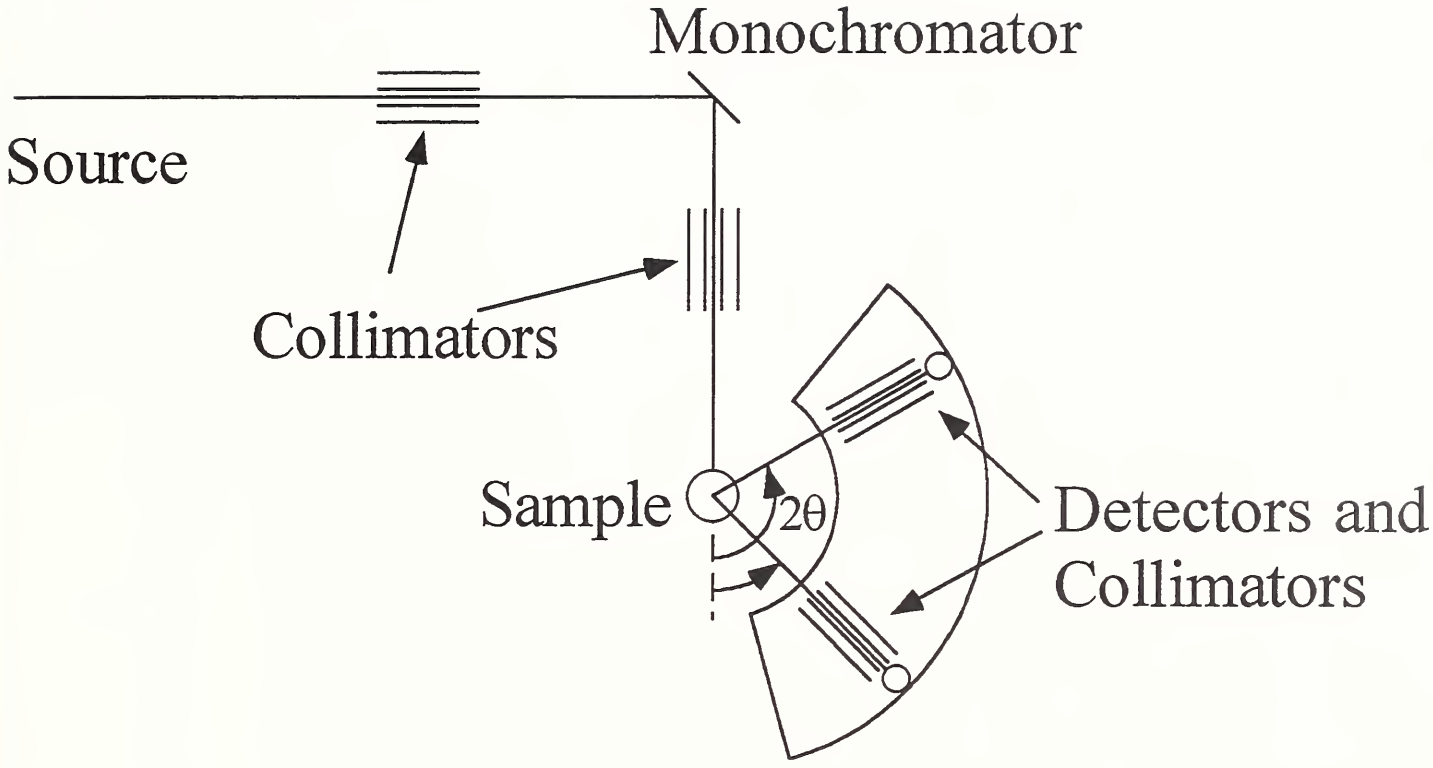
Monochromator
Source
Collimators
Sample
2θ
Detectors and
Collimators

Fig.2

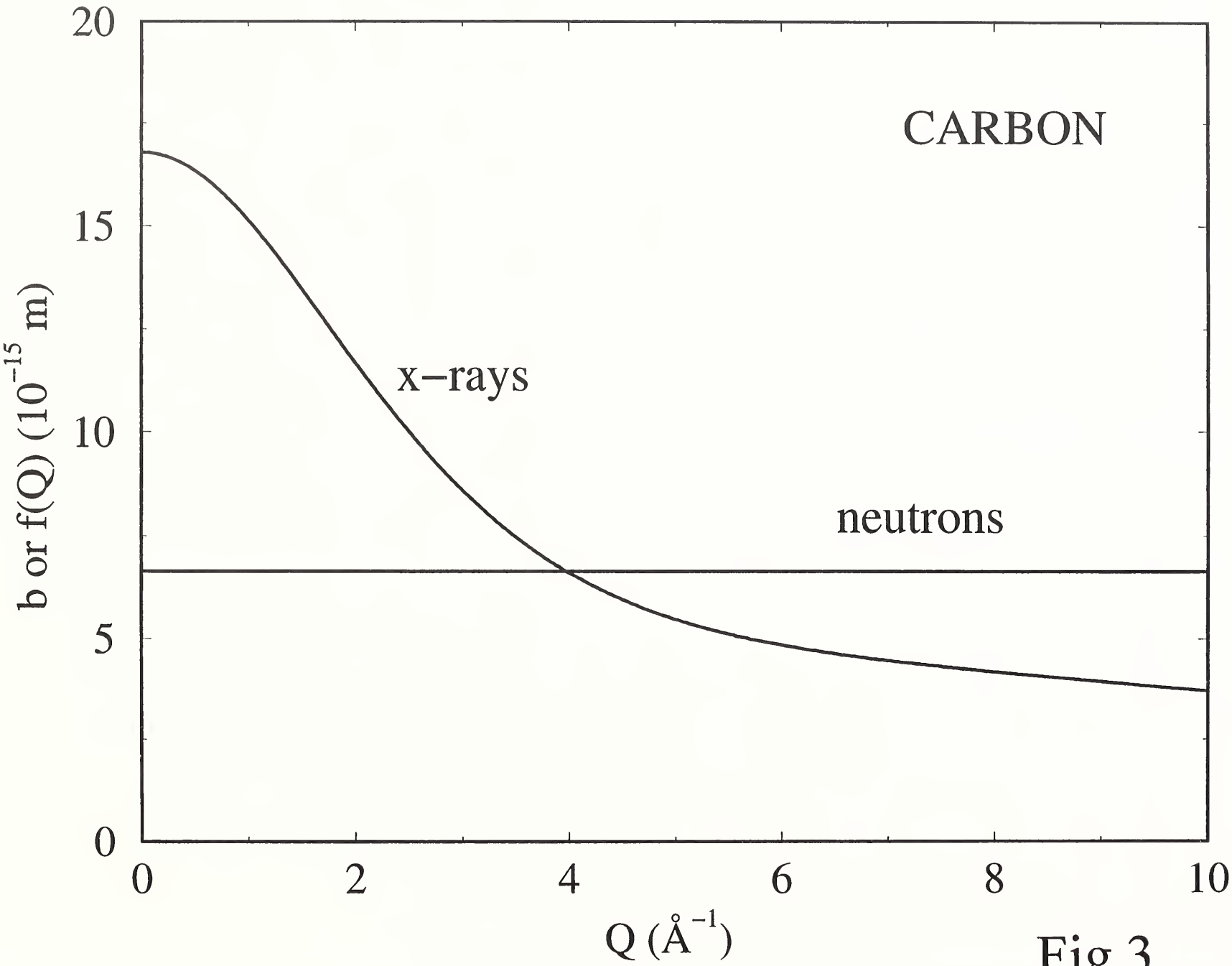

Fig.3

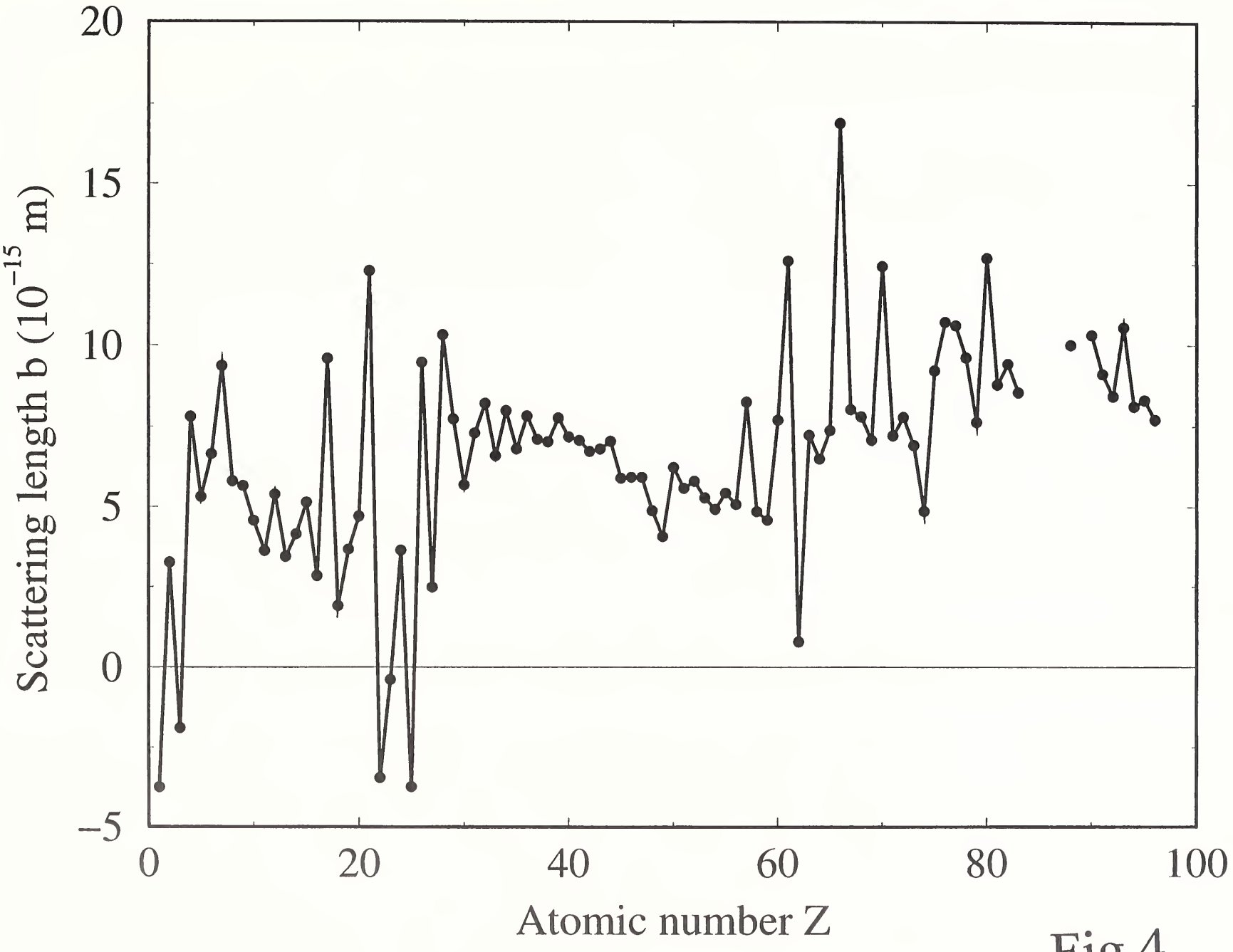
20
15
10
5
0
−5
Scattering length b (10^{-15} m)
0
20
40
60
80
100
Atomic number Z

Fig.4

Closed Cycle Helium Gas Refrigerator

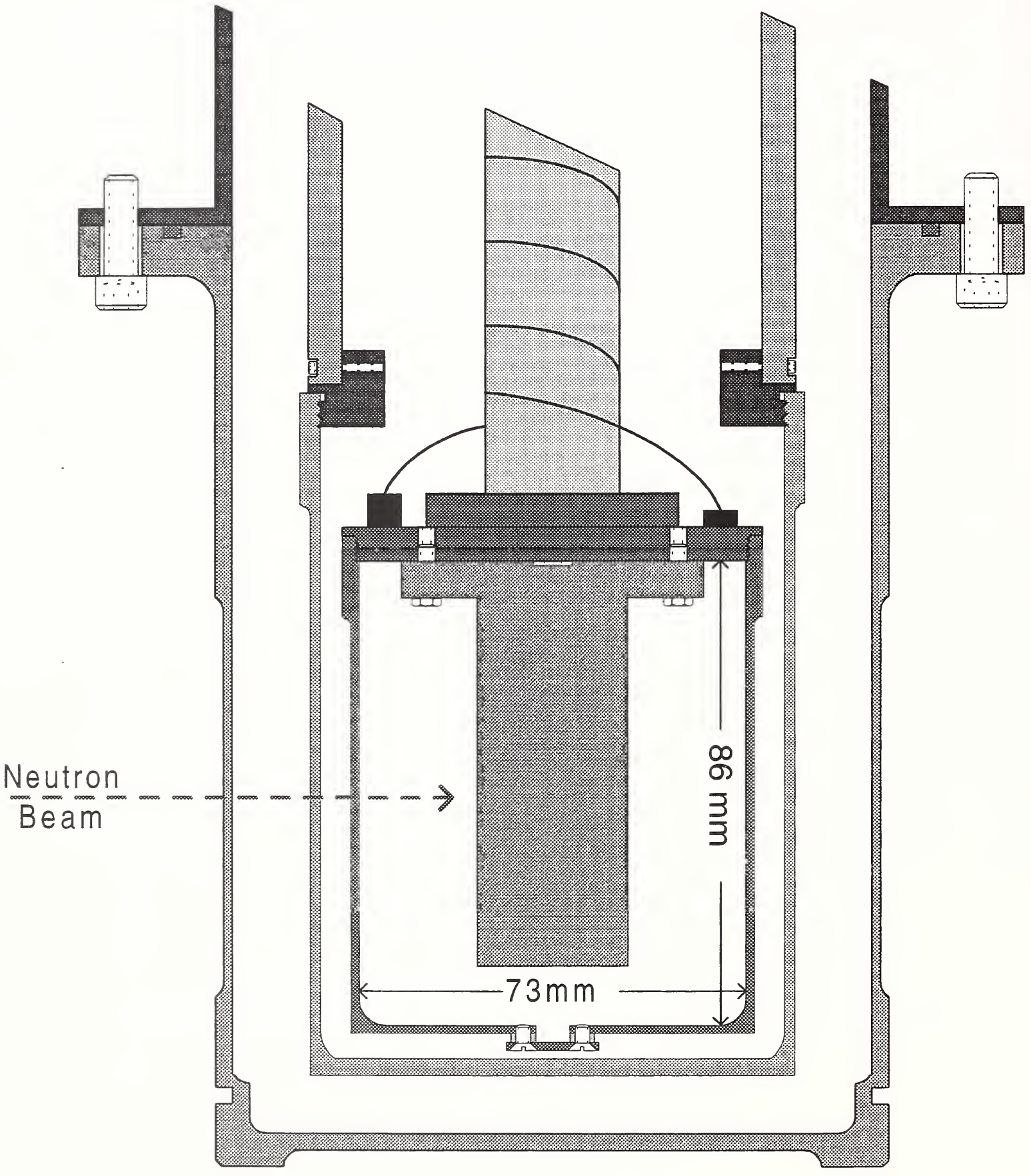

Fig.5 (a)

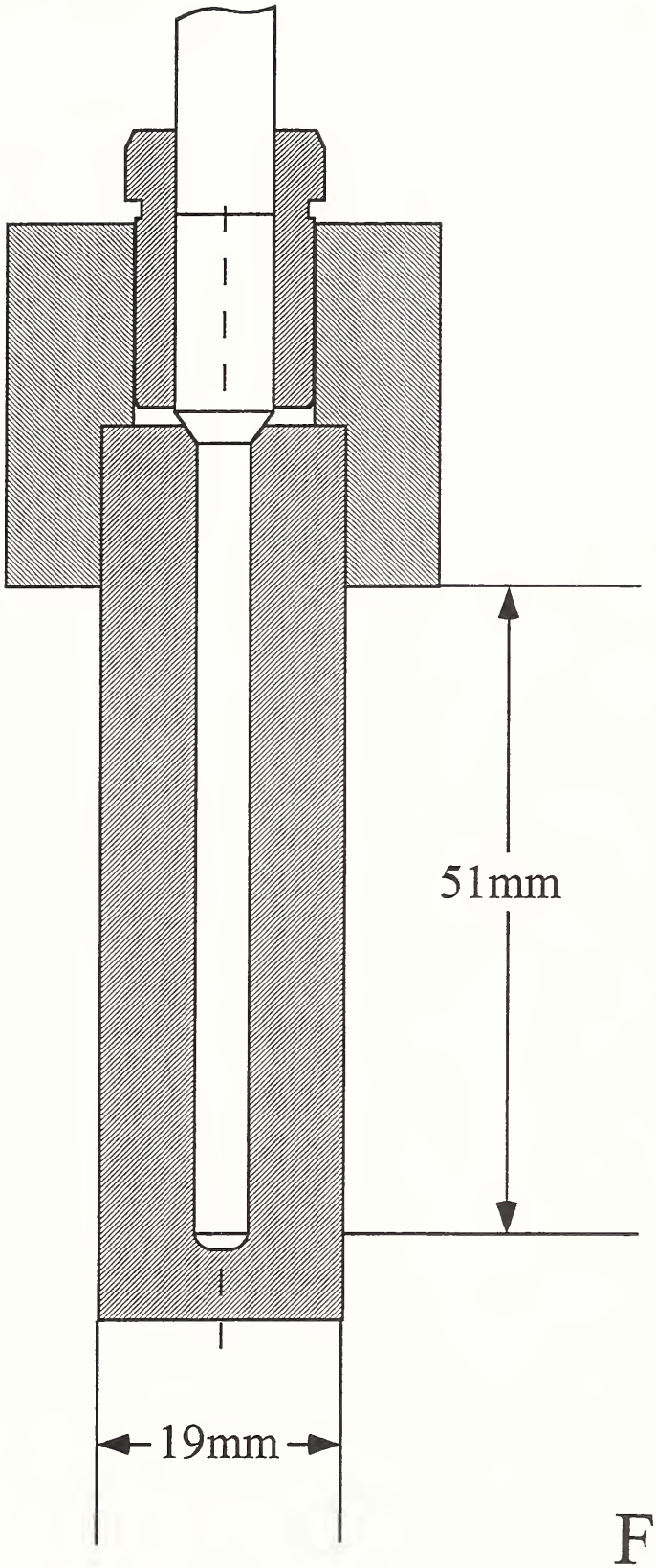

Fig. 5(b)

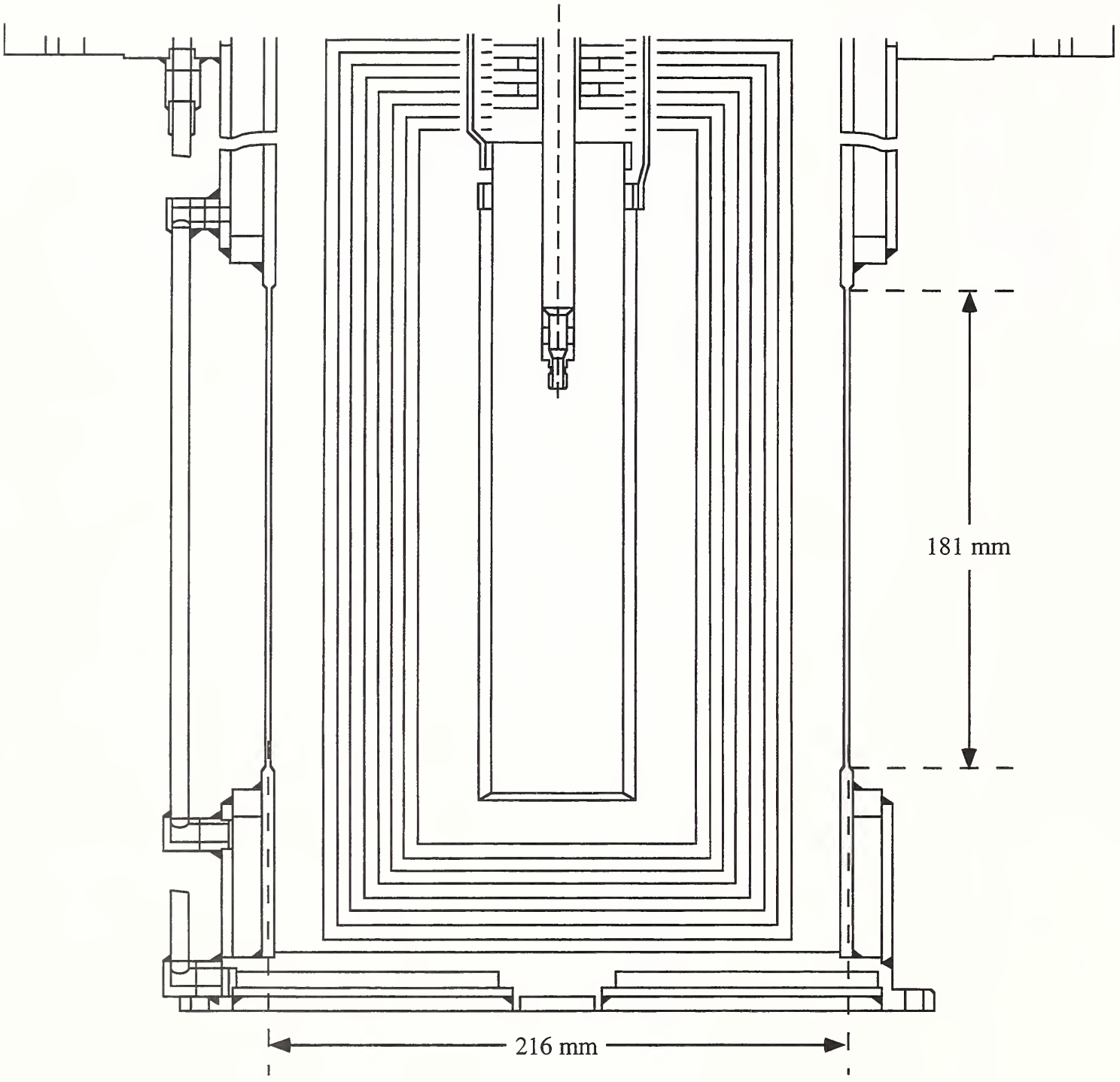

Fig.5(c)

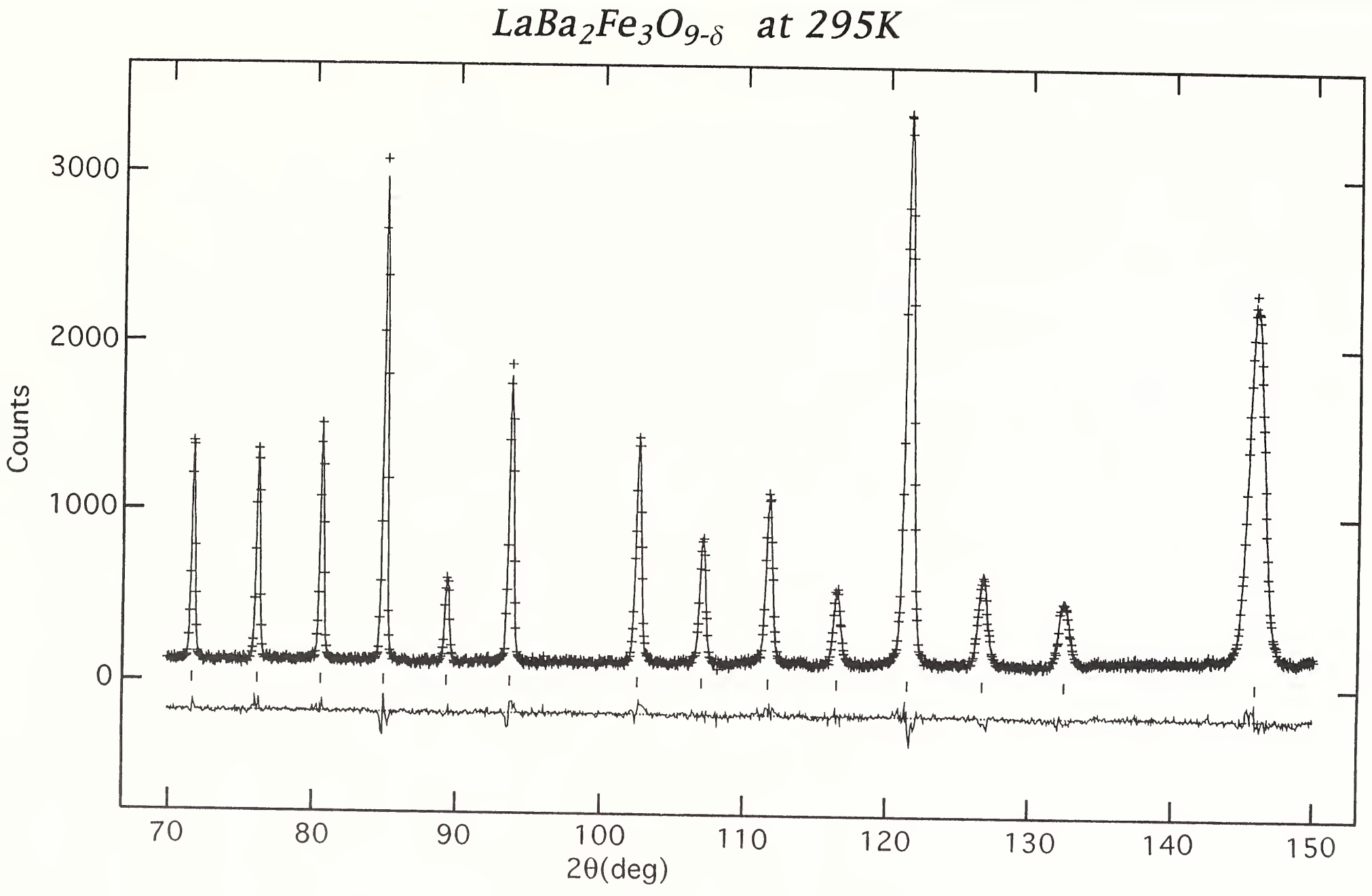
$LaBa_2Fe_3O_{9-\delta}$ at 295K
3000
2000
1000
0
Counts
70
80
90
100
110
120
130
140
150
2θ(deg)

Fig.6

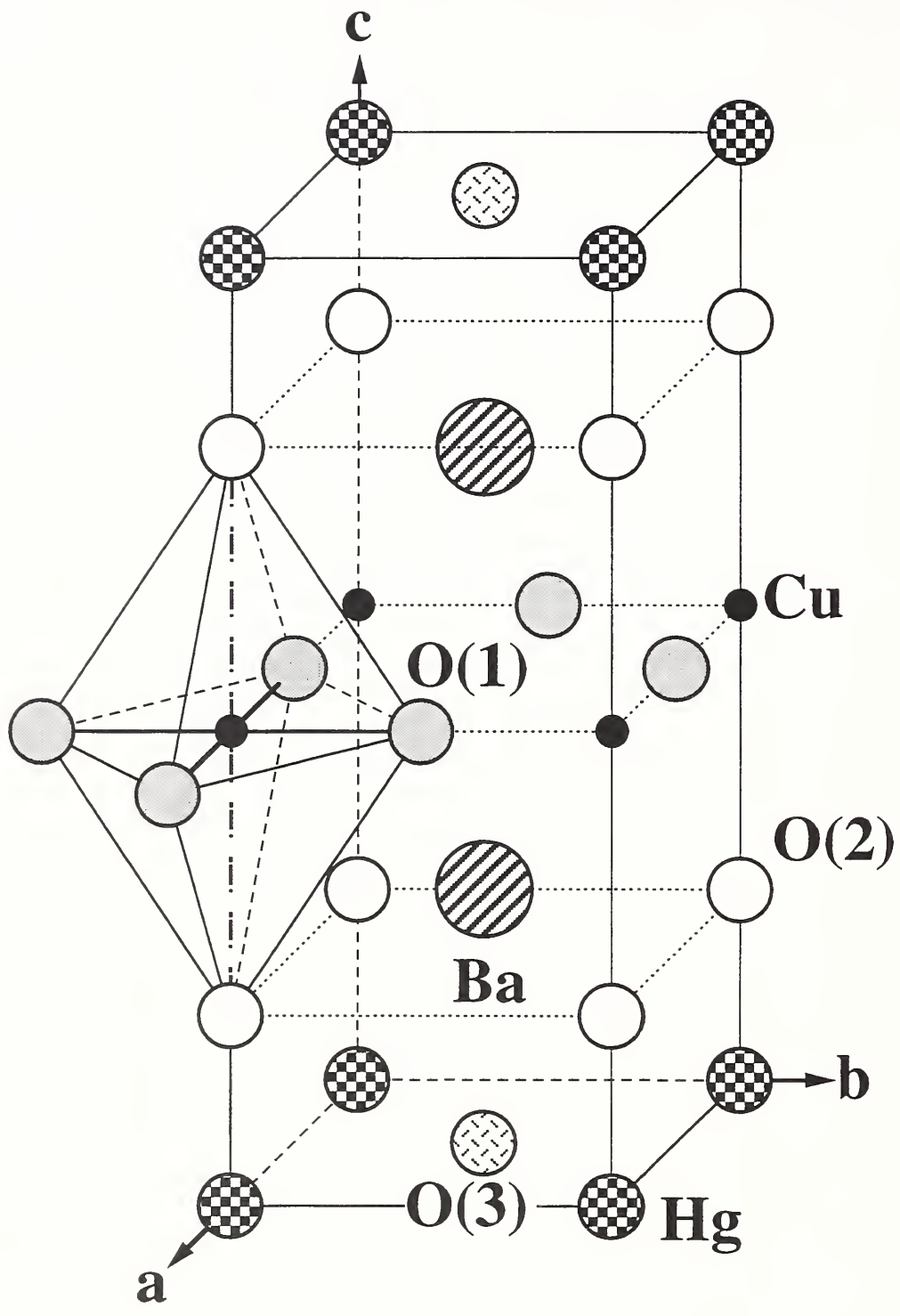

Crystal structure of $HgBa_2CuO_{4+\delta}$

Fig.7

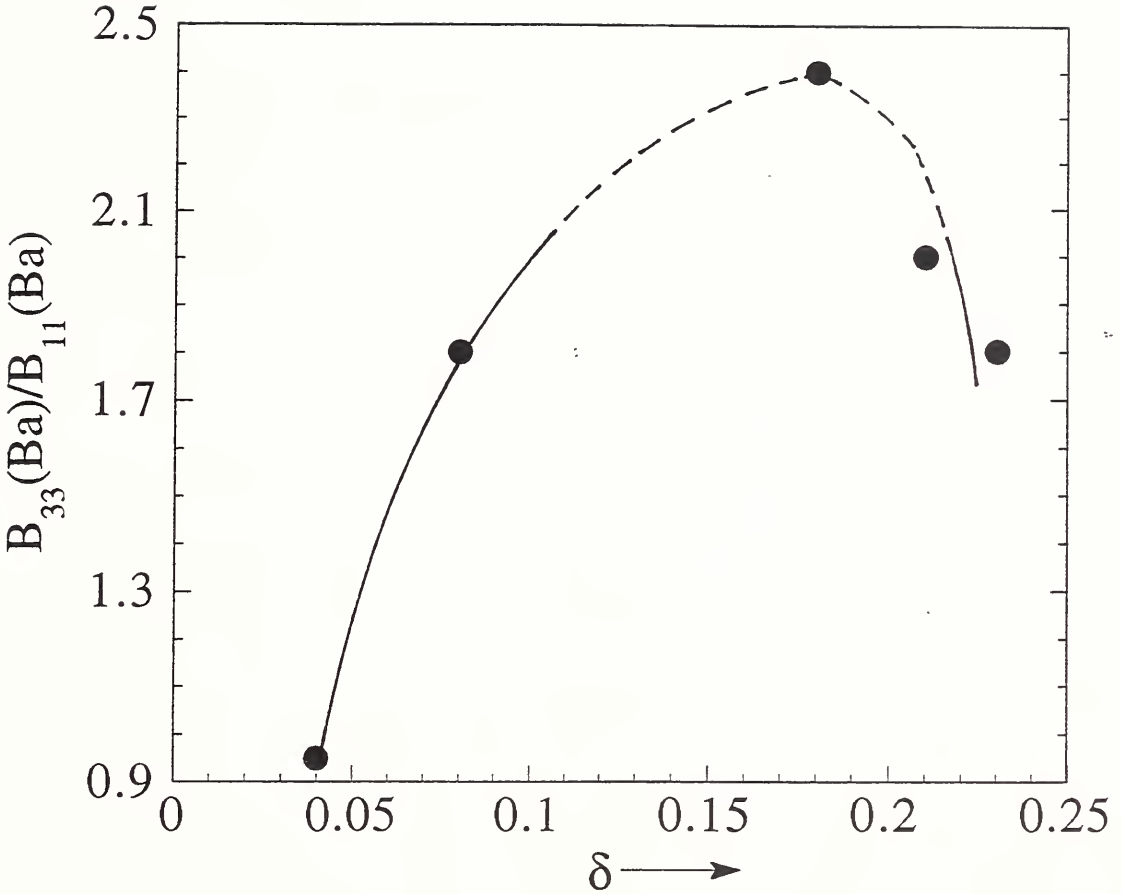
2.5
2.1
1.7
1.3
0.9
$B_{33}(Ba)/B_{11}(Ba)$
0
0.05
0.1
0.15
0.2
0.25
δ

(a)

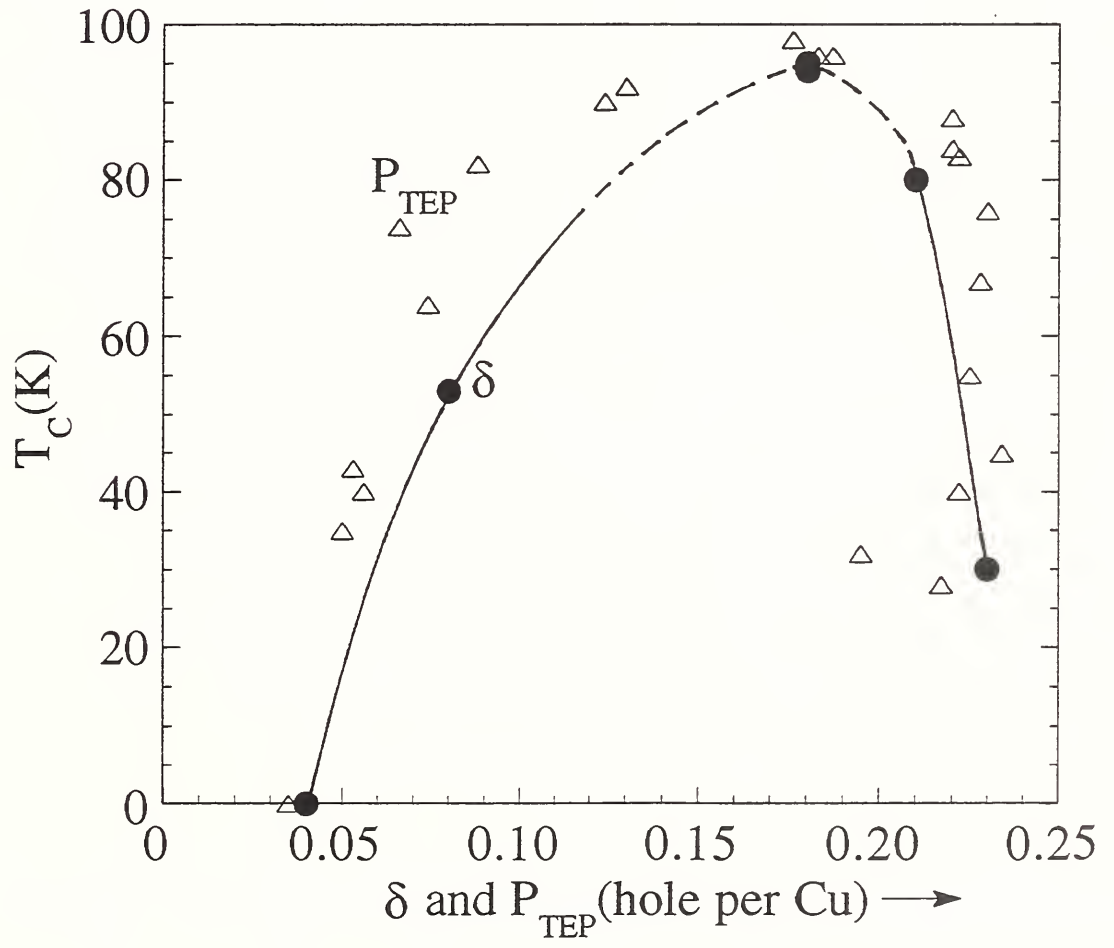
100
80
60
40
20
0
$T_C(K)$
P_{TEP}
δ
0
0.05
0.10
0.15
0.20
0.25
δ and P_{TEP}(hole per Cu)

(b)

Fig.8

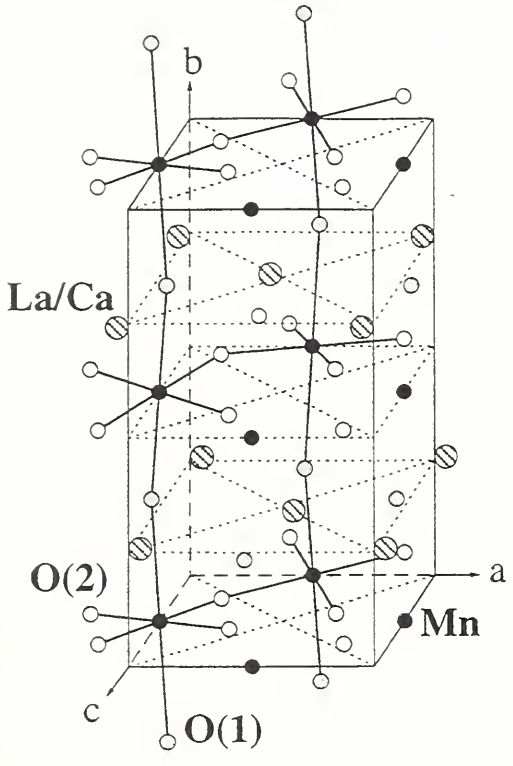

(a)

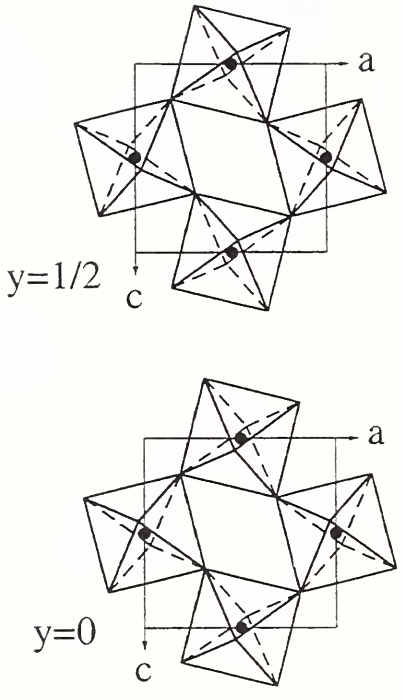

(b)

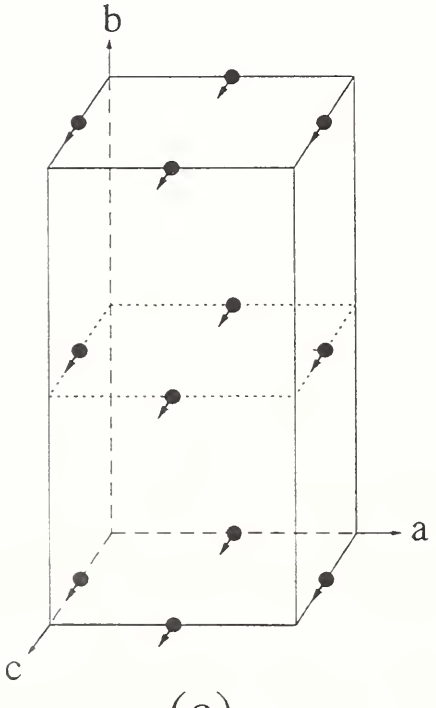

(c)

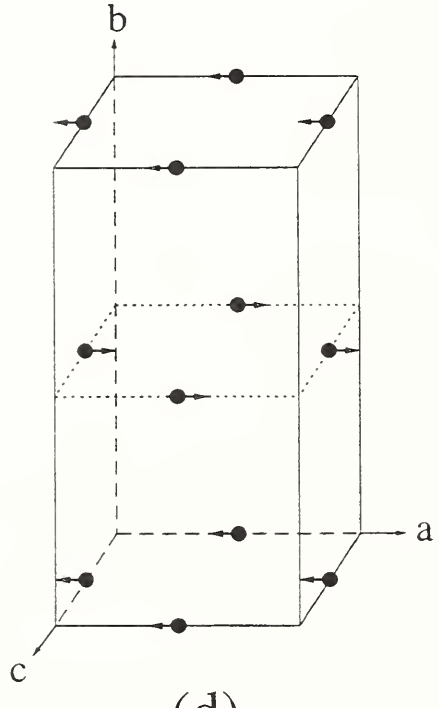

(d)

Nuclear and magnetic structures of $La_{1-x}Ca_xMnO_3$.

Fig.9

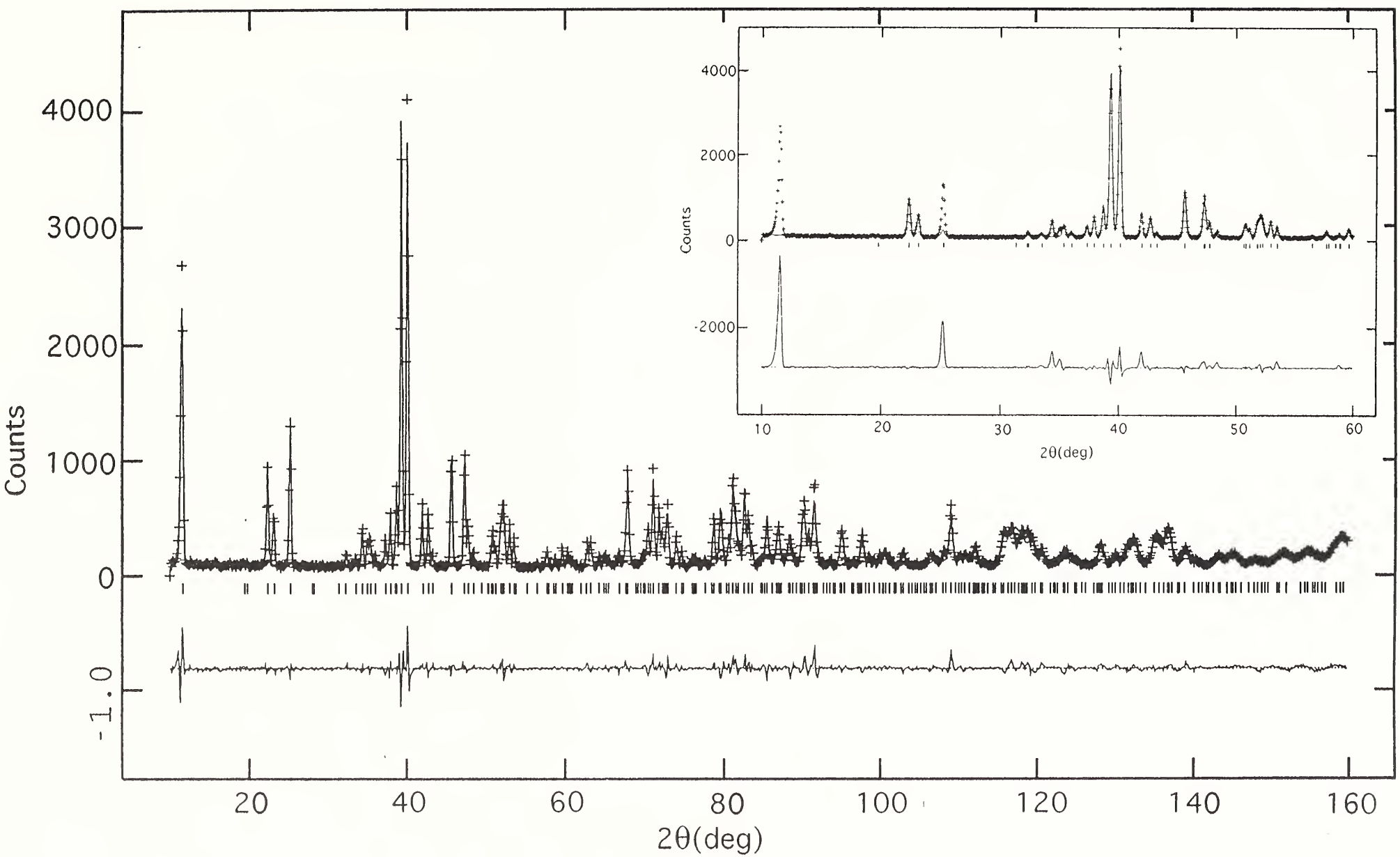
$La_{0.94}Ca_{0.06}MnO_3$ at 12K, Antiferromagnetic order.
Counts
4000
3000
2000
1000
0
-1.0
20
40
60
80
100
120
140
160
2θ(deg)
4000
2000
0
-2000
Counts
10
20
30
40
50
60
2θ(deg)

Fig.10

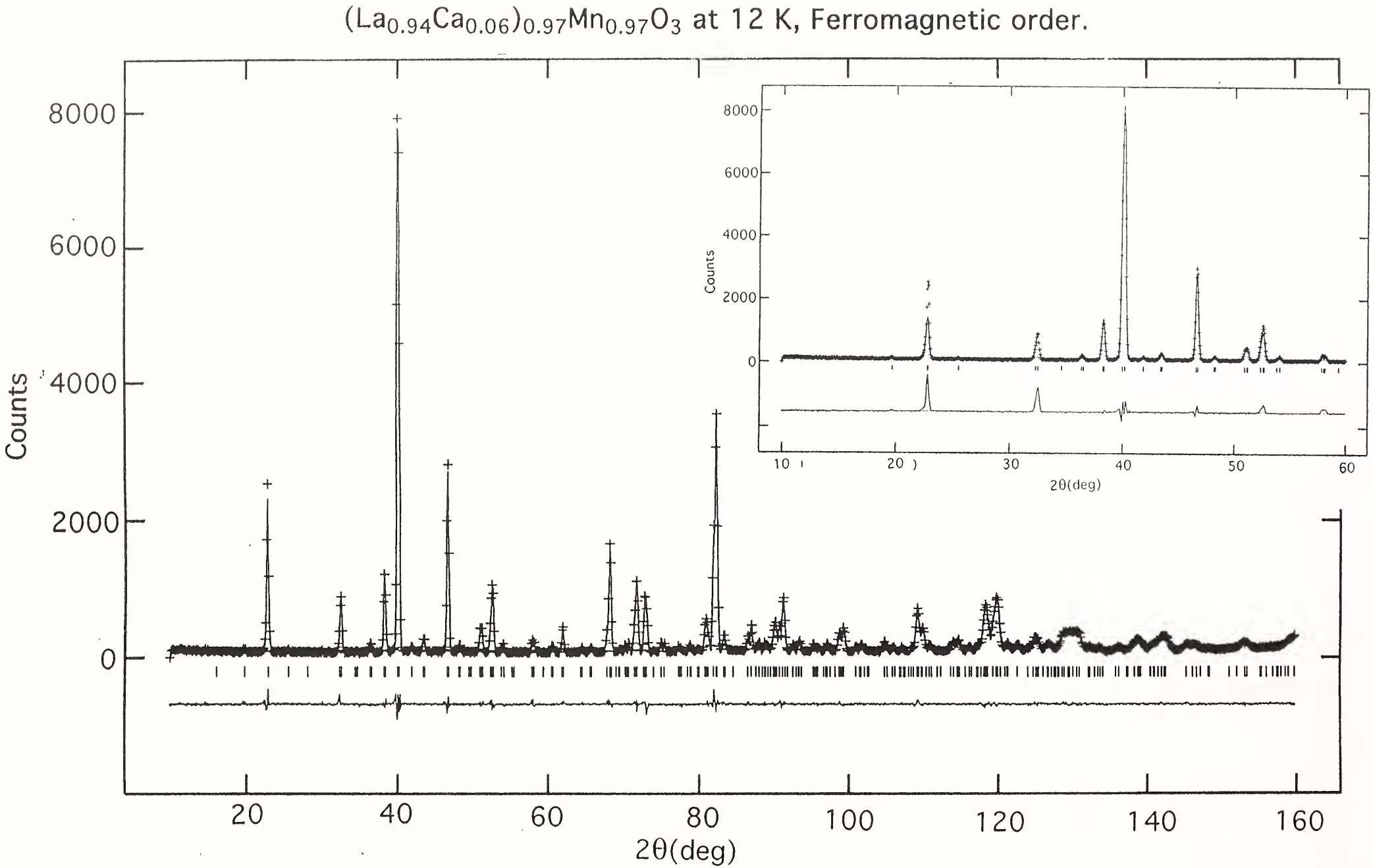
$(La_{0.94}Ca_{0.06})_{0.97}Mn_{0.97}O_3$ at 12 K, Ferromagnetic order.
Counts
8000
6000
4000
2000
0
20
40
60
80
100
120
140
160
2θ(deg)
Counts
8000
6000
4000
2000
0
10
20
30
40
50
60
2θ(deg)

Fig.11

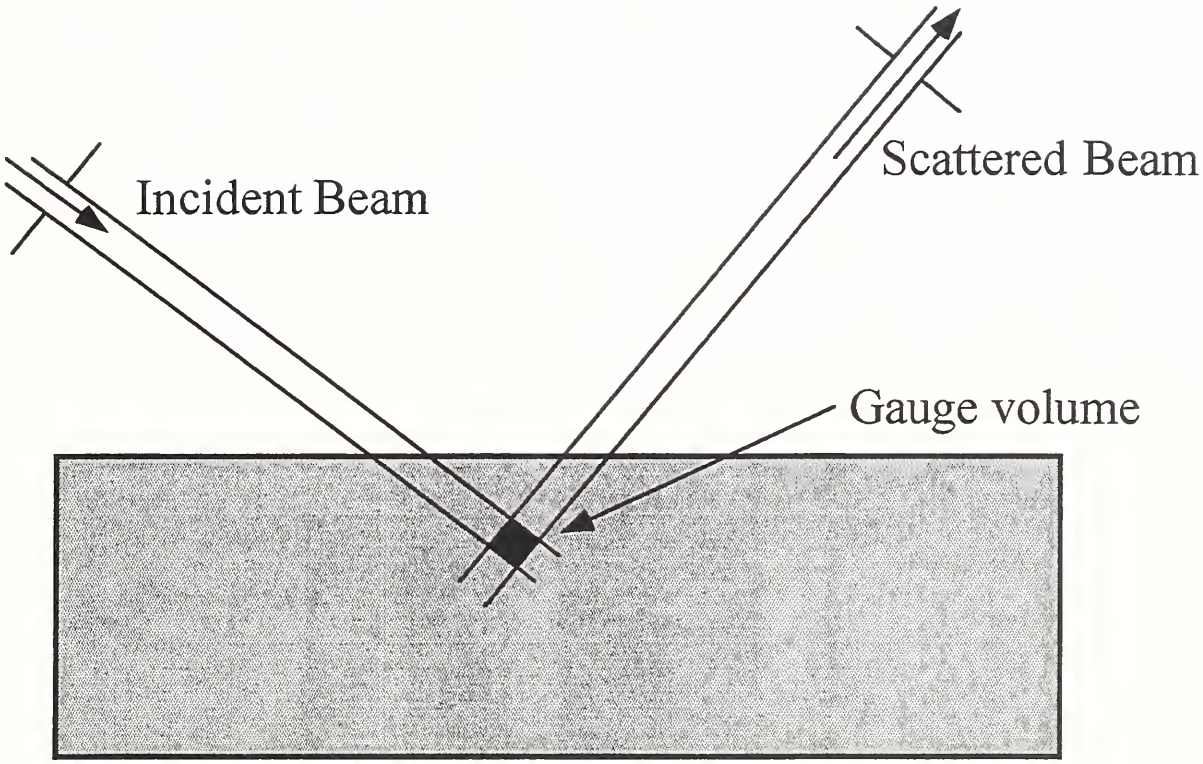

Fig.12

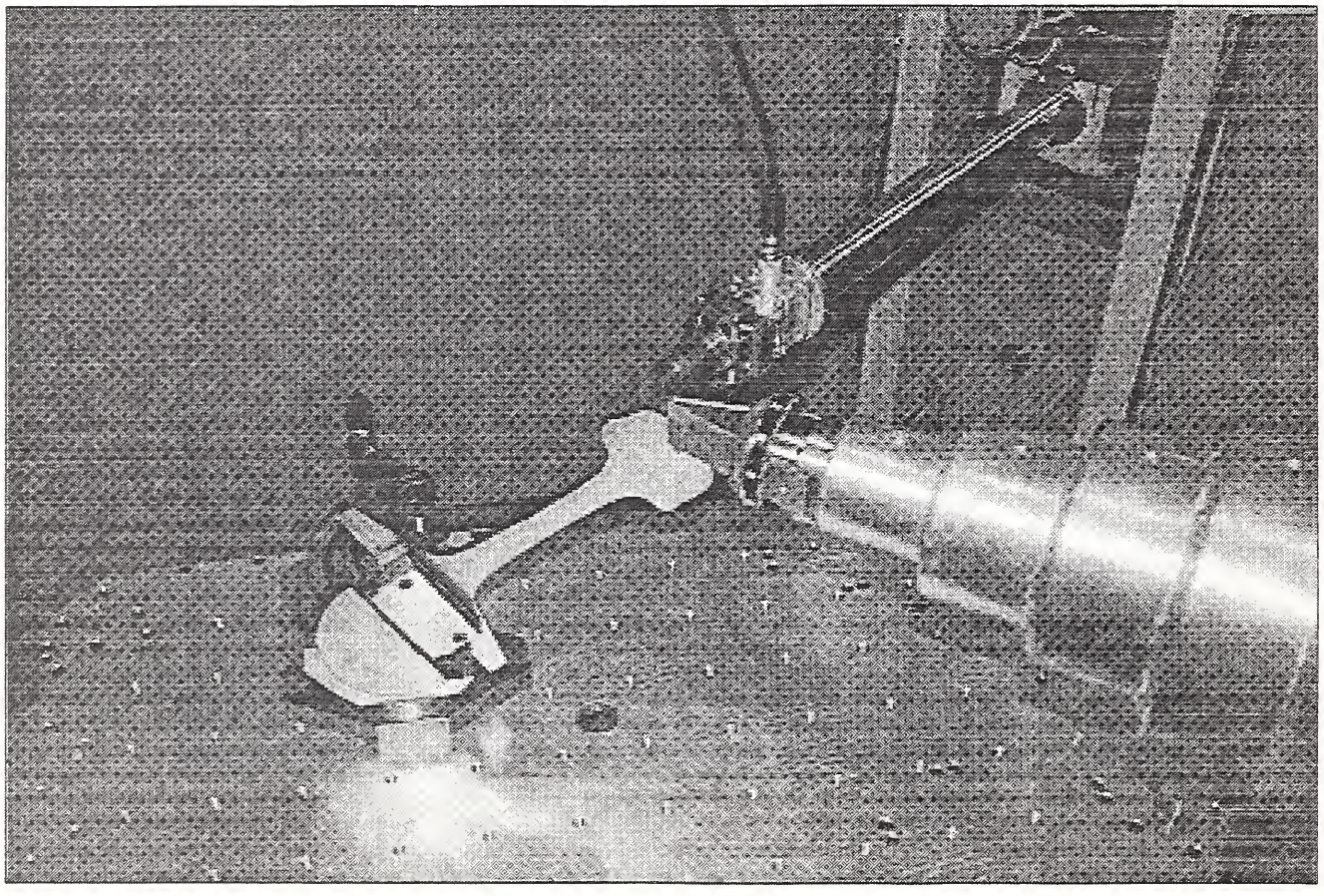

Fig.13

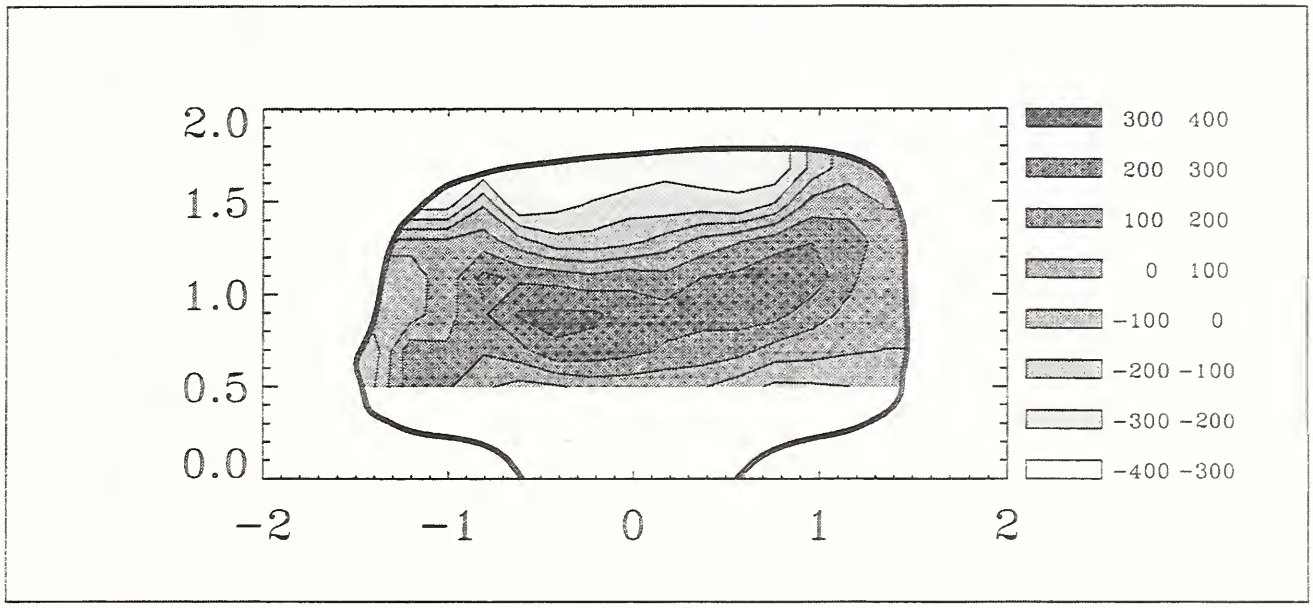
2.0
1.5
1.0
0.5
0.0
−2
−1
0
1
2
300 400
200 300
100 200
0 100
−100 0
−200 −100
−300 −200
−400 −300

Fig.14

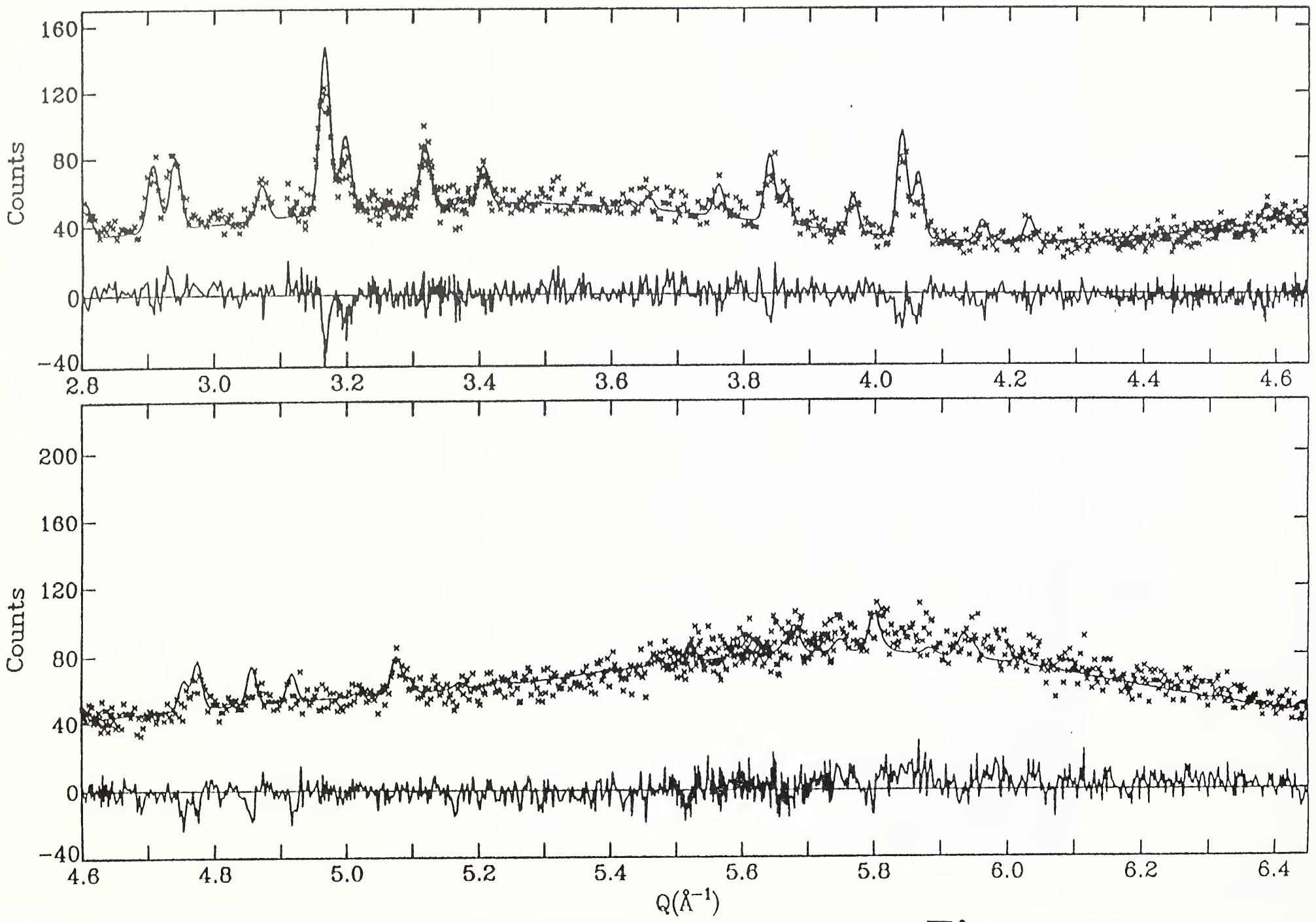
Counts
160
120
80
40
0
-40
2.8
3.0
3.2
3.4
3.6
3.8
4.0
4.2
4.4
4.6
Counts
200
160
120
80
40
0
-40
4.6
4.8
5.0
5.2
5.4
5.6
5.8
6.0
6.2
6.4
Q(Å^{-1})

Fig.15

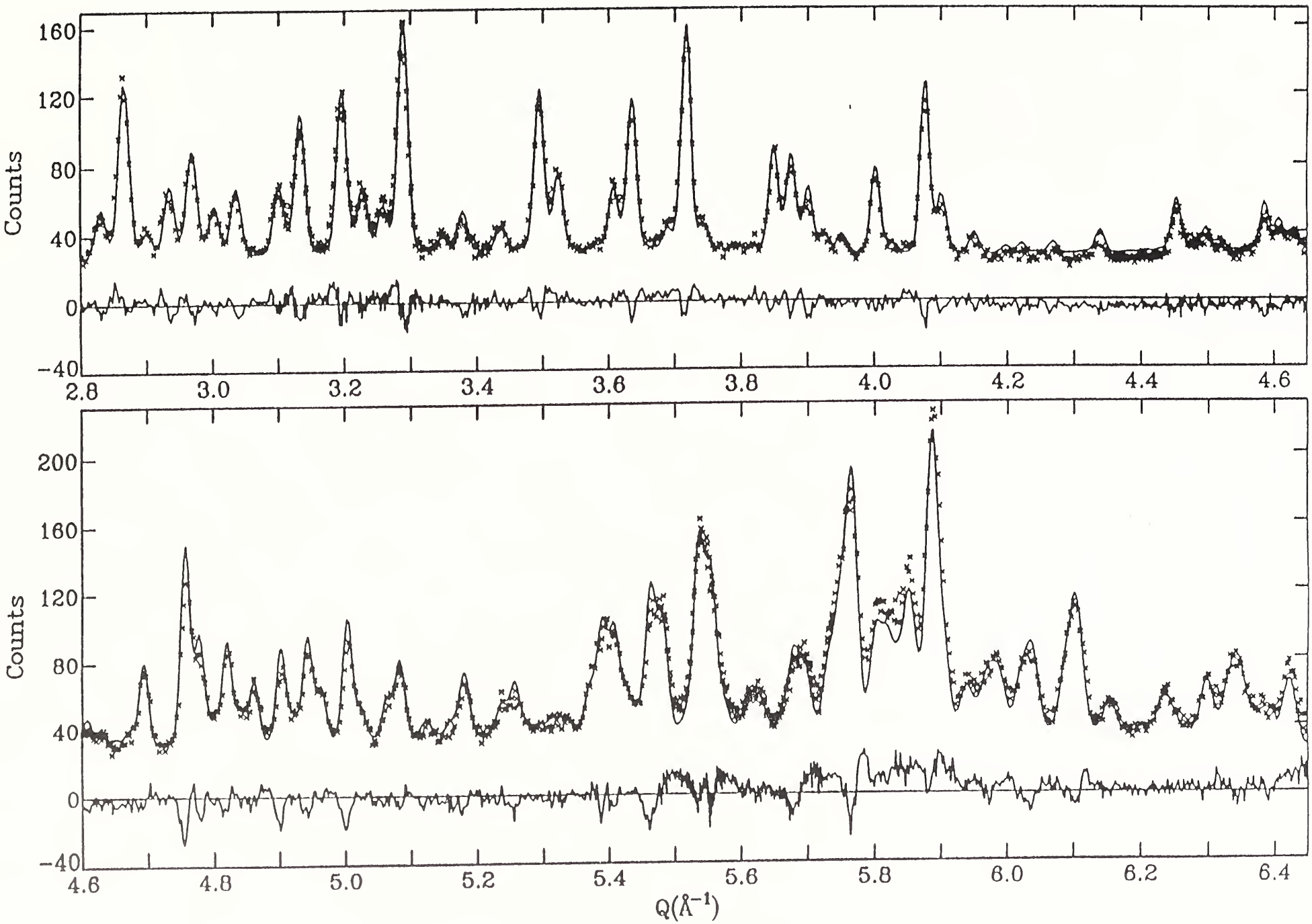
Counts
160
120
80
40
0
-40
2.8
3.0
3.2
3.4
3.6
3.8
4.0
4.2
4.4
4.6
Counts
200
160
120
80
40
0
-40
4.6
4.8
5.0
5.2
5.4
5.6
5.8
6.0
6.2
6.4
Q(Å^{-1})

Fig.16

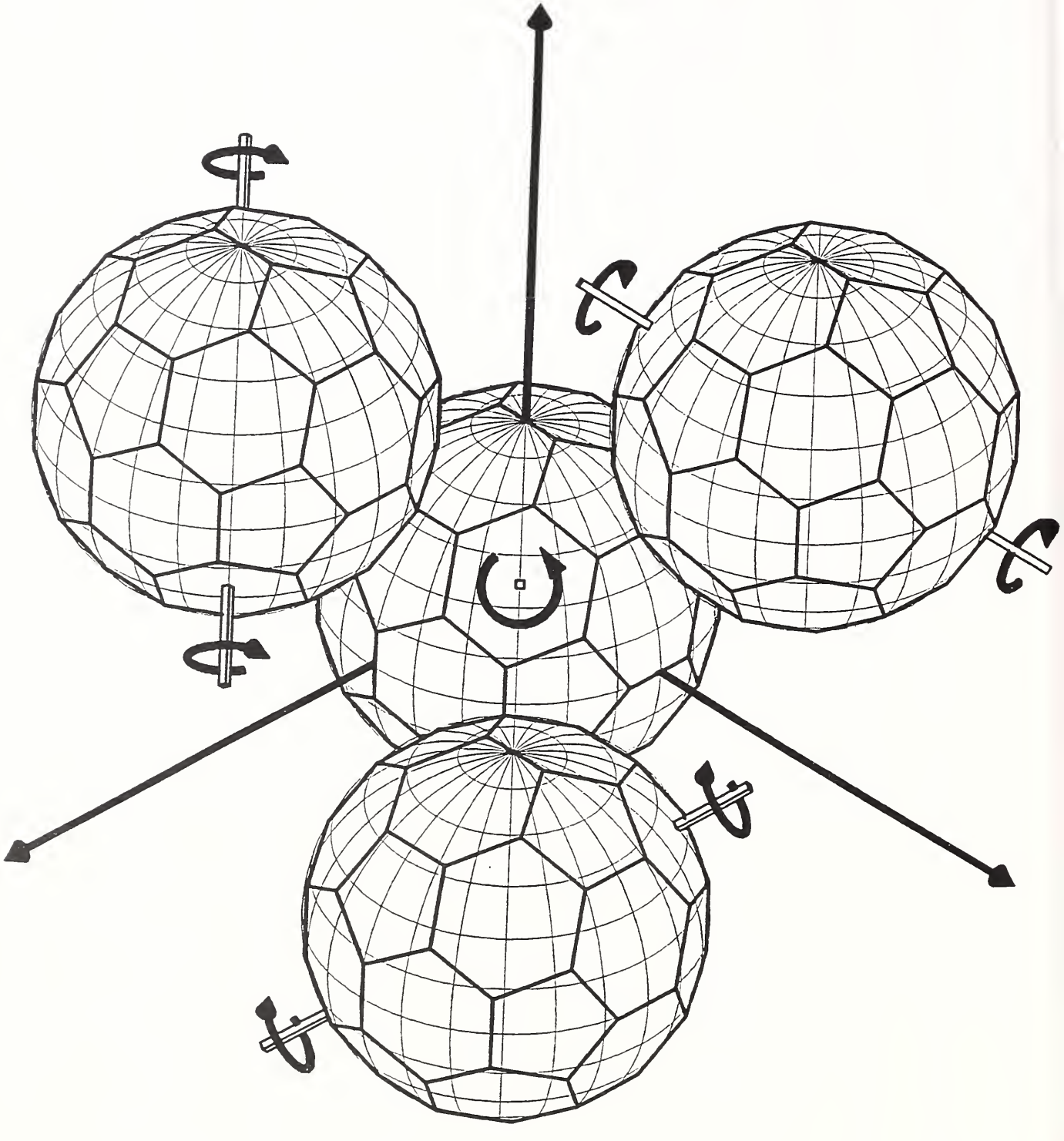

Fig.17

(a)

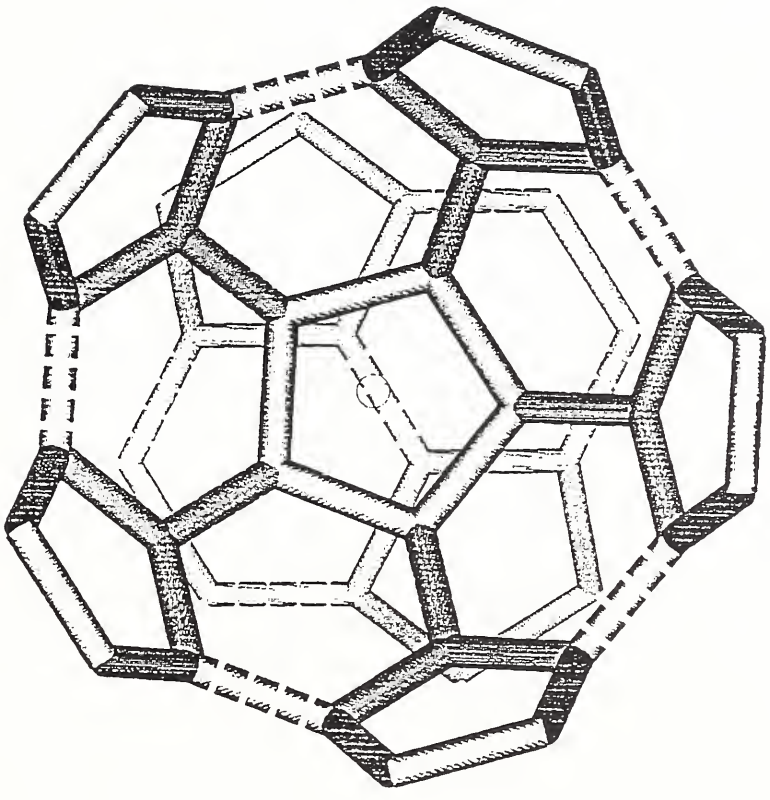

(b)

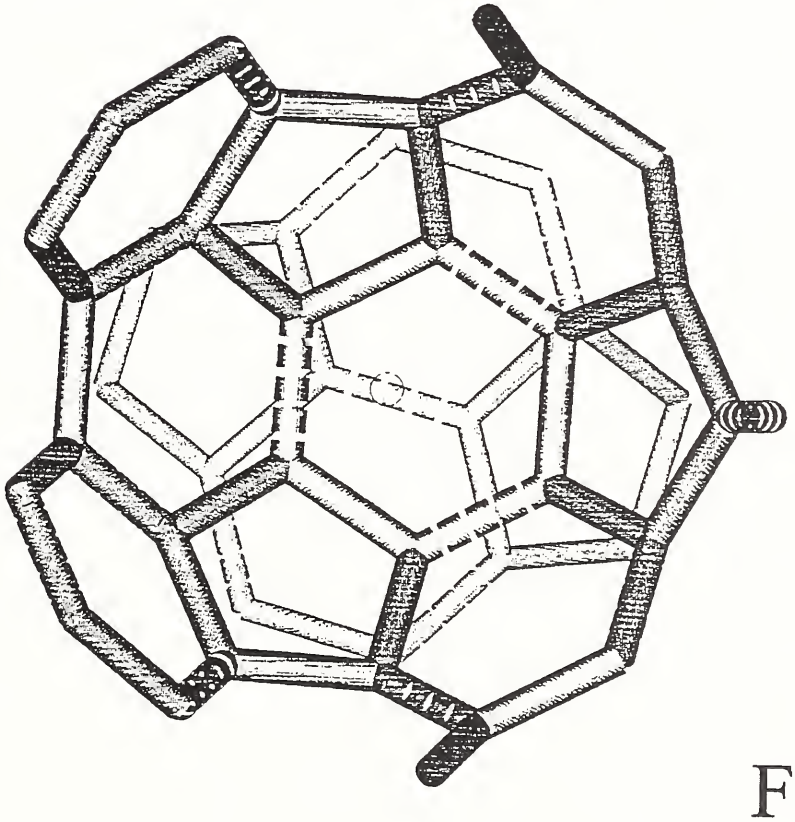

Fig.18

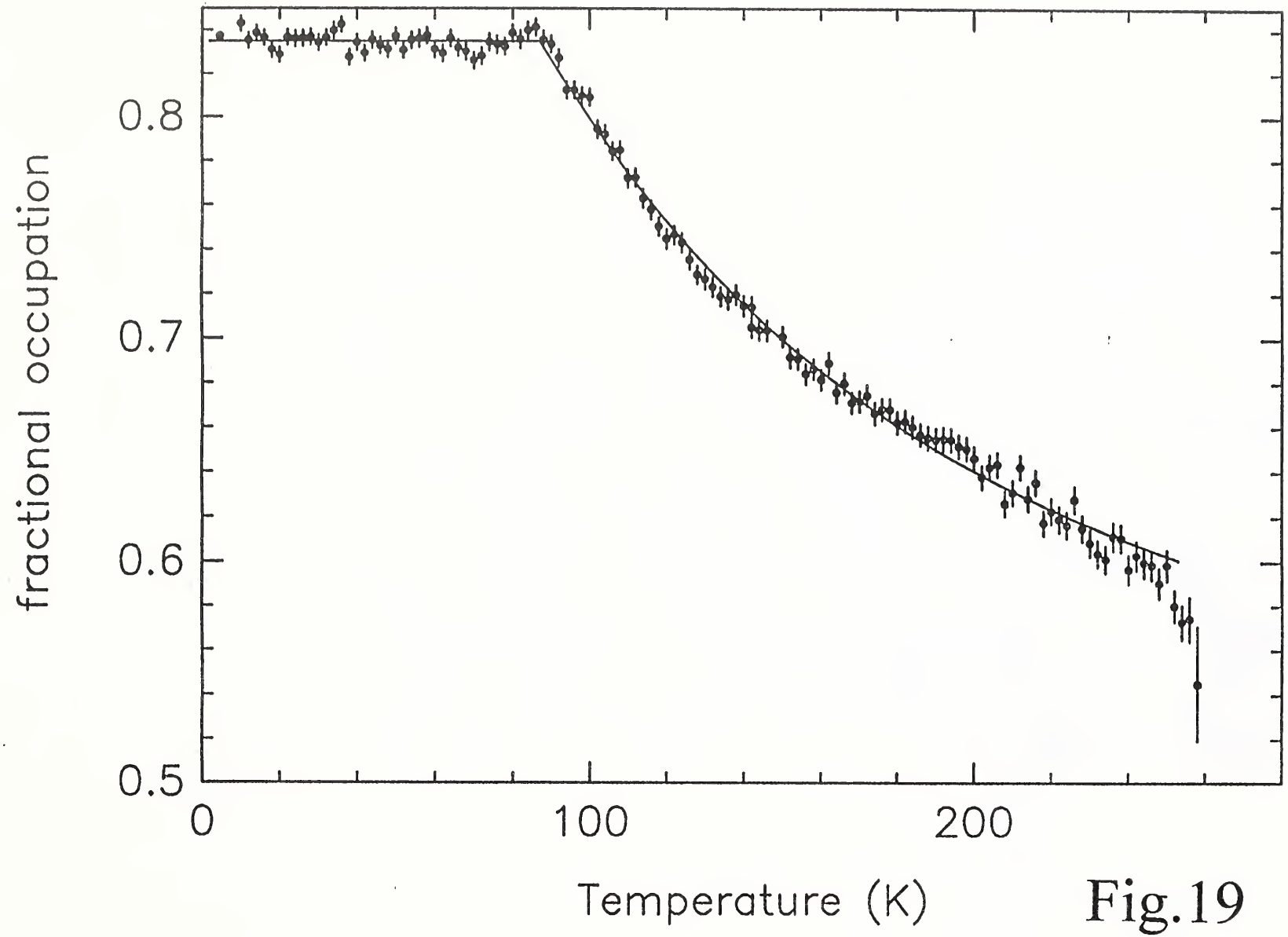

Fig.19